UNCLASSIFIED
SECURITY CLASSIFICATION OF THIS PAGE

MASTER COPY - FOR REPRODUCTION PURPOSES

(2)

REPORT DOCUMENTATION PAGE

AD-A205 866

DTIC ELECTE MAR 22 1989 S H

	1b. RESTRICTIVE MARKINGS
	3. DISTRIBUTION/AVAILABILITY OF REPORT Approved for public release; distribution unlimited.
4. PERFORMING ORGANIZATION REPORT NUMBER(S)	5. MONITORING ORGANIZATION REPORT NUMBER(S) ARO 22450.1-CH
6a. NAME OF PERFORMING ORGANIZATION Brooklyn College of CUNY	6b. OFFICE SYMBOL (If applicable)
	7a. NAME OF MONITORING ORGANIZATION U. S. Army Research Office
6c. ADDRESS (City, State, and ZIP Code) Brooklyn, NY 11210	7b. ADDRESS (City, State, and ZIP Code) P. O. Box 12211 Research Triangle Park, NC 27709-2211
8a. NAME OF FUNDING/SPONSORING ORGANIZATION U. S. Army Research Office	8b. OFFICE SYMBOL (If applicable)
	9. PROCUREMENT INSTRUMENT IDENTIFICATION NUMBER DAAG29-85-K-0118
8c. ADDRESS (City, State, and ZIP Code) P. O. Box 12211 Research Triangle Park, NC 27709-2211	10. SOURCE OF FUNDING NUMBERS PROGRAM ELEMENT NO. / PROJECT NO. / TASK NO. / WORK UNIT ACCESSION NO.

11. TITLE (Include Security Classification)
Preparation, Characterization and Performance of MoS_3 as an Active Cathode Material

12. PERSONAL AUTHOR(S)
Prof. Fred H. Pollak

13a. TYPE OF REPORT	13b. TIME COVERED	14. DATE OF REPORT (Year, Month, Day)	15. PAGE COUNT
Final	FROM 6/15/85 TO 12/14/88	Feb. 14, 1989	63

16. SUPPLEMENTARY NOTATION
The view, opinions and/or findings contained in this report are those of the author(s) and should not be construed as an official Department of the Army position, policy, or decision, unless so designated by other documentation.

17. COSATI CODES		
FIELD	GROUP	SUB-GROUP

18. SUBJECT TERMS (Continue on reverse if necessary and identify by block number)
Cathode materials, Molybendum Trisulfide.

19. ABSTRACT (Continue on reverse if necessary and identify by block number)

We report on a program of the preparation, characterization and performance of amorphous MoS_3 (a-MoS_3) as an active cathode material. We have, for the first time, prepared thin films (~1μm of a-MoS_3). This was accomplished by electrodeposition from both aqueous and non-aqueous solutions of $(NH_4)_2MoS_4$ (ATTM) at room temperature. These thin films were studied by several experimental methods including x-rays, Raman

20. DISTRIBUTION/AVAILABILITY OF ABSTRACT ☐ UNCLASSIFIED/UNLIMITED ☐ SAME AS RPT. ☐ DTIC USERS	21. ABSTRACT SECURITY CLASSIFICATION Unclassified
22a. NAME OF RESPONSIBLE INDIVIDUAL	22b. TELEPHONE (Include Area Code) / 22c. OFFICE SYMBOL

DD FORM 1473, 84 MAR — 83 APR edition may be used until exhausted. All other editions are obsolete.

SECURITY CLASSIFICATION OF THIS PAGE
UNCLASSIFIED

(1)

cont'd

scattering, optical transmission and electrolyte electroreflectance. From the transmission and electrolyte electroreflectance measurements we have, for the first time, evaluated the fundamental energy gap (1.1eV to 1.2 eV) of this semiconductor material. In addition we have developed the technique of nuclear reaction analyis (NRA) as a primary tool to determine the lithium content in a-MoS_3Li_x. Prior to this work only one secondary technique. the measurement of the total charge density during the charge/discharge cycle was available for evaluating the Li concentration.

Various electrochemical measurements also were undertaken. We find the Li capacity of our thin film a-MoS_3 to be comparable to a-MoS_3 prepared in bulk powder form. However, all previous electrochemical measurements have not been performed on pure a-MoS_3 since the powder plus binder was used as the active cathode. Also it is possible to perform charge/discharge measurements much more rapidly on thin films in relation to previous bulk, mechanism of electrodeposit. It was found that the equilibrium between $(NH_4)_2MoS_4$ and a-MoS_3 is shifted to deposition of MoS_3 by the electrochemical oxidation of reduced sulfur to polysulfide.

Keywords:

ARO 22450.1-CH

PREPARATION, CHARACTERIZATION AND PERFORMANCE OF MoS_3 AS AN ACTIVE CATHODE MATERIAL

FINAL REPORT

PROFESSOR FRED H. POLLAK

FEBRUARY 14, 1989

U.S. ARMY RESEARCH OFFICE

CONTRACT #DAAG 29-85-K-0118

BROOKLYN COLLEGE OF CUNY

TABLE OF CONTENTS

I. INTRODUCTION

Of all the candidates as a lithium active cathode, MoS_3 offers perhaps the most interesting possibilities. Early work on chemical incorporation of lithium by n-butyl lithium indicates that as many as 4 lithiums/Mo can be inserted.[1,2] The initial electrochemical discharge in a lithium battery indicated that from 3.4 to 3.8 Li/Mo can be inserted. A calculation from the discharge potential of 1.9V for three lithiums gives an energy density of 715 W/Kg. This type of energy density is far superior to that calculated for any of the other chalcogenide systems. Molybendium trisulfide is also of interest since, along with $MoSe_3$, WS_3 and WSe_3, it can be prepared only in the amorphous form.

In this project we have undertaken the preparation and characterization of amorphous MoS_3(a-MoS_3). We have for this first time prepared thin films (~1μm) of a-MoS_3. This was accomplished by electrodeposition from both aqueous and non-aqueous solutions of $(NH_4)_2MoS_4$(ATTM) at room temperature. These thin films were studied by several experimental methods including X-rays, Raman scattering, optical transmission and electrolyte electroreflectance. From the transmission and electrolyte electroreflectance measurements we have, for the first time, evaluated the fundamental energy gap (1.1eV to 1.2eV) of this semiconductor material. In addition we have developed the techniques of nuclear reaction analysis (NRA) as a primary tool to determine the lithium content in a-MoS_3Li_x. Prior to this work only one secondary technique, the measurement of the total charge density during the charge/discharge cycle was available for evaluating the Li concentration.

Various electrochemical measurements also were undertaken. We find the Li capacity of our thin film a-MoS_3 to be comparable to a-MoS_3 prepared in bulk powder form. However, all previous electrochemical measurements have not

been performed on pure a-MoS_3 since the powder plus binder was used as the active cathode. Also it is possible to perform charge/discharge measurements much more rapidly on thin films in relation to previous bulk, pwder samples. Cyclic voltammetry studies gave important insights into the mechanism of electrodeposit. It was found that the equilibrium between $(NH_4)_2$ MoS_4 and a-MoS_3 is shifted to deposition of MoS_3 by the electrochemical oxidation of reduced sulfur to polysulfide.

II. PREPARATION

In this project we have for the first time prepared thin films of a-MoS_3.[3,4] These films were typically about 1 micron thick. They were prepared by electrodeposition from both non-aqueous (NA) and aqueous (A) solutions of $(NH_4)_2MoS_4$ at room temperature. Methanol and water were used as the NA and A solvents, respectively.

Prior to his work two techniques have been used by previous research groups to prepare amorphous MoS_3.[5,6] Both of these techniques are based on the decomposition of a precursor compound $(NH_4)_2MoS_4$; they both produce bulk powders and not thin films. These bulk powders can be prepared from the thermal decomposition of $(NH_4)_2MoS_4$ or the acid decomposition of an aqueous solution of $(NH_4)_2MoS_4$. Recently, Auborn et al reported the preparation of a-MoS_3 powder by various electrochemical precipitation methods.[7]

For the electrodeposition process we employed an IBM Instruments Inc., EC/225-3a voltammetric analyzer. The bath consisted of an 0.04M ammonium tetrathiomolybdate solution in methanol (NA) or water (A). The thin films were deposited from both NA and A solutions in the potential range +0.3V to +1.5V (vs SCE) employing Pt as a counterelectrode. Various current densities

were used. We designate the a-MoS_3 films electrodeposited from a non-aqueous solvent as ED-MoS_3(NA) and the a-MoS_3 thin films electrodeposited from an aqueous solvent as ED-MoS_3(A).

Substrates used for both types of ED-MoS_3 were indium tin oxide (ITO) thin films on glass. The substrates were carefully degreased and rinsed with methanol followed by a nitrogen gas drying. Careful cleaning of the substrates was found to be essential for the uniformity of the ED-MoS_3 thin films.

Film thickness in the range from 0.05μm to 1μm were obtained by varying the deposition time period between 5-90 minutes.

For comparison we have also prepared a-MoS_3 by the thermal decomposition of ammonium tetrathiomolybdate powder at 200C in nitrogen gas atmosphere.[6] We designated this material as TD-MoS_3. From the a-MoS_3 powder we made pressed pellet samples of TD-MoS_3 at a pressure of 6 tons/cm^2.

Crystalline MoS_2 powder was prepared by heating a Mo and S mixture in the proper ratio at 700C under vacuum for 5 days in a silica tube. We designated this material as c-MoS_2. Crystalline MoS_2 pellet samples were prepared from the powder at 6 tons/cm^2 pressure.

Thin films of μc-MoS_2 were prepared by heating ED-MoS_3 (NA) thin films at 500C in nitrogen gas. It is known[8] that heating a-MoS_3 at temperatures above 350°C causes the loss of one sulfer atom resulting in the formation of MoS_2, either in crystalline (c) of poorly crystallized (px) form.[8,9] We find that our procedure results in px-MoS_2 rather than c-MoS_2.

III. CHARACTERIZATION

A. Raman scattering

Raman scattering was employed to characterize the various materials.[3] Raman spectra were recorded at room temperature on a Spex model 1401/14018 double grating monochromator with a cooled photomultiplier tube (Products for Research, Inc. Model 9498-31). The backscattering geometry was used for all the measurements. The excitation light source was the 5145A line of an Ar-ion laser (Coherent Radiation CR-6, model 53 head).

Shown in Fig. 1 are the Raman spectra in the range 140-690 cm^{-1} from an ED-MoS_3(NA) sample (solid line), an ED-MoS_3(A) sample (dotted line) and a TD-MoS_3 sample (dashed line) at laser power densities of 50mW/cm^2, 50mW/cm^2 and 20mW/cm^2, respectively. Five bands, designated at A,B,C,D and E are clearly evident. The observed five features are located in the range between 150-160 cm^{-1} (band A), 210-220 cm^{-1} (band B), 300-360 cm^{-1} (band C), 425-450 cm^{-1} (band D), 520-550 cm^{-1} (band E), respectively. The Raman spectra of the ED-MoS_3 and TD-MoS_3 samples are quite similar and agree with the spectrum reported earlier by Chang and Chan[8] for a-MoS_3 made by the thermal decomposition technique, i.e. TD-MoS_3. The similarity of both ED-MoS_3 Raman spectra with that of TD-MoS_3 (including Ref. 5), which is known to be amorphous, is a strong indication of the amorphous nature of our ED-MoS_3 thin films. The bands C and E have been identified with Mo-S and S-S stretching modes, respectively. The low Rayleigh scattering of the ED-MoS_3(A) in comparison with the ED-MoS_3(NA) indicate good surface morphology for former thin films.

Figure 2 shows the Raman spectra of c-MoS_2 (dotted line) and px-MoS_2 (dashed line) at the laser power density of 300 mw/cm^2. Peaks at 386 cm^{-1} and at 408 cm^{-1} are observed from c-MoS_2 while px-MoS_2 produces peaks at 380 cm^{-1} and 405.5 cm^{-1}. Raman peaks of c-MoS_2 have been reported[8] at 384 cm^{-1} and 408 cm^{-1}. The slight shift and broadening of the μc-MoS_2 Raman features in

relation to c-MoS_2 could be due to either microcrystalline effects or strains in the thin films.[10] The most important point to note is that the Raman peaks of a-MoS_3 (see Fig. 1) and MoS_2 (either c-MoS_2 or px-MoS_2) are located in very different spectral regions. Since we have not observed any MoS_2 peaks in the a-MoS_3 Raman spectra (see Fig. 1) we conclude that the ED-MoS_3 (NA, A) and TD-MoS_3 prepared in our laboratories do not have significant MoS_2 contamination.

B. X-ray Diffraction

X-ray diffraction data were taken for both ED-MoS_3 (NA) and ED-MoS_3 (A) samples. X-ray diffraction data were obtained using a Philips 3100 x-ray generator with CuK_α radiation. No X-ray diffraction line was obtained from either type of ED-MoS_3 thin films, thus further confirming the amorphous nature of the thin films.

C. Optical Transmission

In order to evaluate the fundamental energy gap we have taken optical transmission spectra at room temperature from ED-MoS_3 thin films (deposited on 80% transmittance ITO layers) in a Cary Model 219 double beam spectrophotometer.[3] We chose ITO as the conducting substrates because it is transparent and thus does not interfere with optical measurement in our wavelength region. Moreover, an ITO substrate was always used as the reference in the double beam spectrophotometer.

Shown in Fig. 3 are typical transmission spectra in the range of 0.8-2.8 eV of two ED-MoS_3 (NA) thin films having thicknesses of 0.18 μm (dotted line) and 0.63 μm (dashed line), respectively. In the range between 1.0-2.8 eV the transmission of both thin films decreases with increasing energy. As

expected, the transmission of the thicker sample (dashed line) decreases more steeply in comparison with the thinner material. The small peaks in the transmission spectra in this region are from the interference effect, the thinner sample (dotted line) showing some distinct interference peaks at 1.3, 1.5 and 2.0 eV. These peaks are less evident when the sample is much thicker (dashed line). The sharp drop in the transmission below 1.0 eV appears to be due to the strong interference effects and not to a real absorption process.

The spectral dependence of the absorption coefficient, $\alpha(\hbar\omega)$, was evaluated from the transmission spectra of the thin films of different thickness by using the following relation:[11]

$$\alpha(\hbar\omega) = (d_2 - d_1)^{-1} \ln [T_1(\hbar\omega)/T_2(\hbar\omega)] \quad (1)$$

where d and T are the film thickness and percent ransmittance, respectively. Using the above procedure we have determined $\alpha(\hbar\omega)$ in the range 1.0-2.8 eV. Evaluation of $\alpha(\hbar\omega$ below 1.0 eV is complicated by the strong interference effects discussed above.

To get a significant average of $\alpha(\hbar\omega)$ for both ED-MoS_3(NA) and ED-MoS_3(A) samples we have used several samples of different thickness for transmission measurements. All samples were prepared using the deposition procedure as described in the experimental details section to provide a meaningful average of d and hence α. Film thicknesses were measured using an Alpha-step profiler (Tencor Instruments).

The fundamental energy gap, E_g, of an amorphous semiconductor can be evaluated from the spectral dependence of $\alpha(\hbar\omega)$ using the following relation:[12]

$$(\alpha\hbar\omega)^{1/2} = A[\hbar\omega - E_g] \quad (2)$$

where A is a constant factor. The optical energy gap can thus be determined by an extrapolation of an $(\alpha\hbar\omega)^{1/2}$ vs. $\hbar\omega$ plot. The plots of $(\alpha\hbar\omega)^{1/2}$ versus $\hbar\omega$ for ED-MoS_3(NA) (solid line) and ED-MoS_3(A) (dotted line) thin films are shown in Fig. 4 in the range 1.0-2.8 eV. The value of $\alpha(\hbar\omega)$ used represents the average over several samples as discussed above. The curves are indeed linear over a considerable range as indicated by the dashed line for both materials. We find that E_g=1.22±0.1 eV(NA), 1.05±0.10 eV(A) and A=242±25$(eV\text{-}cm)^{-1/2}$ (NA), 280±25$(eV\text{-}cm)^{-1/2}$ (A). Representative error bars for $(\alpha\hbar\omega)^{1/2}$ are shown in Fig. 4. The above value of A for a-MoS_3 are comparable to that found for other amorphous semiconductors.[13,14] The shoulder in the optical absorption, below 1.4 eV (NA) and 1.2 eV (A), could be the Urbach tail and/or interference effects and is a subject of further investigation.

D. Electrolyte Electroreflectance

The EER technique[15,16] has also been used to evaluate the energy gap of these materials. Electroreflectance spectra were recorded at 300 K. A nonaqueous propylene carbonate solution was used as the electrolyte and Pt as the counter-electrode. The applied ac modulation voltage was nominally between 20-60V, peak-to-peak at a frequency of 250 Hz. The EER lineshapes were found to be independent of the modulation voltage in this range, indicating operation in the "low-field" regime.

Shown in Fig. 5 are the EER spectra of an ED-MoS_3(NA) sample (solid line), and ED-MoS_3(A) sample (dotted line). Only one broad peak is observed at 1.35±0.10 eV for ED-MoS_3 (NA) and at 1.25±0.10 eV for ED-MoS_3(A).

The arrows (A) and (NA) at the bottom of Fig. 5 indicate the positions of the optical gap evaluated from the optical transmission measurements for ED-MoS_3 (A) and ED-MoS_3(NA) thin films, respectively (see Fig. 4). Similar

small differences in the evaluation of E_g by these two methods has also been observed in a-Si.[15]

It is noticeable that the optical gap of ED-MoS_3 (A) obtained from both EER and optical transmission measurements has shifted towards lower energy in comparison with ED-MoS_3 (NA). It is also noticeable that the half-width of the EER spectra for ED-MoS_3 (A) (0.12 ev) has decreased in comparison with the half-width of ED-MoS_3 (NA) (0.25 ev). These differences between ED-MoS_3 (NA) and ED-MoS_3 (A) could be due to the different local disorder in amporphous network resulting from different preparation conditions. Similar results have been reported for a-Si where a-Si were prepared at different substrate temperatures.[17]

For comparison, EER experiments were also performed on MoS_2 samples (crystalline and poorly crystallized). Shown in Fig. 6 is the EER spectrum of c-MoS_2 in the range 1.5 eV to 4.5 eV. The structures have been labeled as A, B, A', B', C, D, α and β using the notation of Ref. 18. The interband energies obtained from the EER experiment are in good agreement with previously reported values, both theoretical and experimental. In Fig. 6 the A feature (1.85 eV) originates from the fundamental gap of MoS_2 while the B feature (2.01 ev) is related to the spin-orbit component. For the purposes of comparison we will focus only on the A, B structures.

Figure 7 shows the EER spectrum of a μc-MoS_2 sample. There is an S-shaped feature in the range 1.7-2.1 eV, indicating an optical transition with an energy of about 1.9 eV.[18] Thus, by comparison with Fig. 6, we identify this structure with the fundamental gap (and possibly spin-orbit component) of poorly crystallized or microcrystalline MoS_2. Note that in Fig. 7 there is no structure at about 1.2-1.4 eV indicating the absence of any appreciable a-MoS_3 in the μc-MoS_2.

The significant difference of the energy gap positions between MoS_3 and MoS_2 (both crystalline and microcrystalline) is the major point here. The Ed-MoS_3 (NA, A) (see Fig. 5) do not show any EER feature which is close to MoS_2, i.e. around 1.9 eV. Thus, from EER we are also able to conclude that our ED-MoS_3 does not contain significant MoS_2 (crystalline or poorly crystallized) contamination.

E. Nuclear Beam Analysis of Lithium in a-MoS_3Li_x

To date, only one secondary technique, the measurement of the total charge density during charge-discharge cycling,[7] has been available for determining Li concentration in amorphous lithium active cathodes such as a-MoS_3. This secondary technique for the determination of Li concentration relies on the measurement of total charge accumulated during the cycling process and on the assumption of uniform distribution of Li in the active cathode material. It is important, therefore, to look for primary techniques for measuring the Li concentration, and to compare with results obtained by the secondary technique, in order to establish reliable calibrations of secondary measurement techniques. Ion-beam analysis,[19] particularly Nuclear Reaction Analysis (NRA) together with Rutherford Backscattering (RBS), can provide the primary analytical technique for Li concentration measurements and impurity identification (if any is inserted during Li insertion) in the active cathode material such as a-MoS_3. In particular, NRA provides a sensitive, direct method of measuring the absolute Li concentration by measuring the γ-ray yield from the $^7Li(p,\gamma)^8Be$ reaction. This reaction has many well-known isolated (narrow and broad) selective resonances at low energies.[19] The narrowest one, occuring at an incident proton energy of 441 KeV, was chosen for our measurements.

In the present work, we have employed a combination of NRA and RBS to obtain reliable measurements of x in a-MoS_3Li_x on several discharged samples of a-MoS_3 prepared under different conditions.[20] The absolute Li concentration was obtained by comparing the γ-ray yields of the a-MoS_3Li_x samples with two standards consisting of LiF and LiCl compounds. We have also performed depth profiling of the Li concentration by measuring the γ-ray yield as a function of incident proton beam energy.

1. Experimental Details

a. Electrode preparation:

Electrodeposited a-MoS_3 thin films were prepared from both aqueous and nonaqueous solutions of ATTM, on either Ni or indium tin oxide [$(In_2O_3)_{0.91}(SnO_2)_{0.09}$ designated (ITO)] substrates. Details of the thin film deposition have been described in earlier publications. The thin films prepared from the non-aqueous methanol solution of ATTM are designated as ED-MoS_3(NA) and the films prepared from the aqueous solution of ATTM are designated as ED-MoS_3(A). The thickness of the films deposited on the ITO and Ni substrates were nominaly 1μm and 2μm, respectively. Pure a-MoS_3 pellets were prepared from a-MoS_3 powder obtained by thermal decomposition of ATTM. Pellets of a-MoS_3 are designated as TD-MoS_3; they are typically 100 μm thick.

b. Electrochemical characterization:

The secondary lithium cells consisted of an a-MoS_3 working electrode (active cathode), lithium metal as the reference electrode and also lighium metal as the counter electrode (anode) in an electrolyte solution of 2 M lithium perchlorate dissolved in propylene carbonate solvent. The electrolyte was purged by argon gas continuously during the lithium insertion processes. The samples of a-MoS_3 after discharging (insertion of lithium) were rinsed

with propylene carbonate solvent to remove any adsorbed lithium perchlorate from the surface and were mounted on a rotating sample holder inside the scattering chamber. A typical lithium insertion curve of an electrodeposited MoS_3 thin film at 100 $\mu A/cm^2$ constant current density is shown in Fig. 8. The lithium concentration in the a-MoS_3 samples was calculated from the total accumulation of charge generated by the lithium insertion ($Li^+ + e^- \rightarrow Li$) reaction. The total accumulated charge was converted to the number of moles by using the well known Faraday's equation where 96,500 coulombs of charge is equivalent to one mole of reactant.

c. Instrumentation:

The electrochemical measurements were carried out with a Princeton Applied Research (PAR) electrochemistry system consisting of a Model 173 potentiostat/galvanostat and a Model 179 digital coulometer.

The nuclear measurements were performed on the Brooklyn College 3.75 MeV Dynamitron Accelerator. The a-MoS_3 samples along with two standards (LiF and LiCl), were mounted on a rotating sample holder inside the scattering chamber. The schematic diagram of the scattering chamber is shown in Fig. 9. The vacuum in the system was maintained at a pressure of 5×10^{-7} torr by turbomolecular and cryogenic pumps along with a liquid nitrogen trap. The RBS spectra were collected by two silicon surface barrier detectors at an angle of 172.5° with respect to the beam. For the NRA analysis, γ-rays of energy 9 to 21 Mev, emitted from the sample, were collected by a 3" x 3" NaI detector, mounted directly above the scattering chamber at a distance of 1/4" from the incident proton beam spot.

2. Results and Discussion

The RBS spectra were collected from the sample to identify the constituent elements in the sample. In RBS spectra, at a known incident beam energy, the energy of the backscattered proton at a depth z, depends on the mass of the target nucleus and the stopping powers as given by the following equations:[21]

$$E' = K[E_o - \Delta E_{in}(z)] - \Delta E_{out}(z) \quad (3)$$

$$K = \{\cos\Theta + [(M/m_p)^2 - \sin^2\Theta]^{1/2}\}^2/[1 + (M/m_p)]^2 \quad (4)$$

where

E' = energy of the backscattered proton,

E_o = Incident beam energy,

$\Delta E_{in}(z)$ and $\Delta E_{out}(z)$ are the energy losses of the beam on the way in and out for a depth z in the sample.

K = kinematic factor,

m_p = mass of proton,

M = mass of the target nucleus,

Θ = scattering angle.

When the sample consists of more than one element, the RBS spectra show several edges corresponding to the characteristic kinematic factors K of the individual elements and the height of each edge is proportional to the elemental amount and its Rutherford cross section.

Figures 10 and 11 show the RBS spectra of the electrodeposited a-MoS_3 thin films on the Ni and ITO substrates, respectively [the spectra are similar for both ED-MoS_3(NA) and ED-MoS_3(A) samples]. Figure 12 shows the RBS spectrum of TD-MoS_3. The RBS spectra of the LiF and LiCl standard samples are shown in Figs. 13 and 14, respectively. In Figs. 10,, 11 and 12 the two front

edges are from Mo and S and the ratio of the edges is in good agreement with MoS_3 stoichiometry. For the Ni-backed ED-MoS_3 the third edge is from the infinitely thick (to the beam) Ni substrate. For ITO-backed ED-MoS_3 the third edge starts from the very thin layer of ITO and falls back when the beam reaches the glass (ITO substrates are prepared by spraying a 1000 A layer of ITO on glass). In Figs. 13 and 14 the front edge is from F and Cl, respectively. Generally we cannot identify any Li edge because of its low mass and small cross section.

In order to determine the Li concentration in the various samples the γ-ray yields from the reaction $^{7}Li\ (p,\gamma)\ ^{8}Be$ occuring at the resonance proton energy of 441 KeV were measured. Figure 15 shows the typical γ-ray spectrum of this resonance reaction. The spectra are similar for both the reference and test samples. The γ-ray window was kept constant for all the measurements.

The absolute Li concentration in a-MoS_3Li_x was obtained by collecting (for a fixed amount of time) and comparing the γ-ray yields from the a-MoS_3Li_x samples with the two standard compounds, i.e., LiF and LiCl.

It is assumed that (a) the sample is uniform over a depth corresponding to the combined width of the resonance plus speed in beam energy due to straggling and (b) the stopping powers (dE/dz) vary only slowly with energy. Then the γ-ray yield is a function only of the atomic stopping cross section (stopping power per molecule) and independent of the sample density. Thus the γ-ray yields (Y_γ) from an a-MoS_3Li_x sample can be represented by the following equation:

$$Y_\gamma(MoS_3Li_x) \propto x/[\epsilon(MoS_3) + x\,\epsilon(Li)] \qquad (5)$$

where

$\varepsilon(MoS_3)$ = stopping power of MoS_3,

$\varepsilon(Li)$ = stopping power of Li.

The yields from LiF or LiCl can be represented by:

$$Y_\gamma(\text{LiCl or LiF}) \propto 1/[\varepsilon(A) + \varepsilon(Li)] \tag{6}$$

where

$\varepsilon(A)$ = stopping power of Cl or F

$\varepsilon(Li)$ = stopping power of Li

The absolute Li concentration related to the ratio (R) of the γ-ray yields of MoS_3Li_x to that of LiF or LiCl was calculated by the following equations:

$$R = Y_\gamma(MoS_3Li_x)/Y_\gamma(\text{LiCl or LiF}) \tag{7a}$$

$$R = x[\varepsilon(A) + \varepsilon(Li)]/[\varepsilon(MoS_3) + x\varepsilon(Li)] \tag{7b}$$

and hence

$$x = R\varepsilon(MoS_3)/[\varepsilon(A) + \varepsilon(Li) - R\varepsilon(Li)] \tag{8}$$

In order to obtain depth profiling of the lithium concentration, the γ-ray yields were measured as a function of incident beam energy. At higher beam energies there will be no γ-yield from the surface but rather from a depth inside the sample where the mean energy of the beam has been brought down to the resonance energy by the energy lost in the sample material. The depth scale was calculated from the energy scale using the stopping power of MoS_3Li_x. Figure 16 shows the energy dependence of the stopping powers of MoS_3Li_x, assuming a constant density of MoS_3 for all x. The depth scale in anstroms of MoS_3Li_x vs the incident beam energy in NMR (units of the magnetic field of the analyzing magnet) displayed in Fig. 17 was obtained by an

integration of the reciprocal of the stopping power of MoS_3Li_x. A molecular beaum of H_2^+ having twice the desired energy (since H_2^+ has twice the mass of H^+) was used in this determination. This procedure was employed since the beam optics of the accelerator gets poor at low energies. Upon hitting the sample the H_2^+ molecular beam breaks up into two protons of the same energy (coulomb explosion) within a few monolayers.

Plotted in Figs. 18 and 19 are the absolute Li concentration (per MoS_3) as a function of depth for samples ED-MoS_3 (NA)/Ni and ED-MoS_3 (NA)/ITO, respectively. Representative error bars are shown in each figure. We find that there is no difference in the spectra for the corresponding thin films prepared from the aqueous (A) solution. Although both of the samples were charged to 3 Li/MoS_3 (see Fig. 8) they have different thicknesses. The former thin film has a thickness of about 2μm while that dimension of the latter is about 1μm. The absolute Li concentration of Figs. 18 and 19, i.e., 3Li/MoS_3, is therefore in very good agreement with the electrochemical conditions. The different depth distributions of Li in the two samples is related to the difference in MoS_3Li_x film thickness, i.e., ED-MoS_3(NA)/Ni is about twice as thick as ED-MoS_3(NA)/ITO.

Shown in Fig. 20 is the absolute Li concentration vs depth of TD-MoS_3. For TD-MoS we have charged different Li concentrations at 100 $\mu A/cm^2$ current density, corresponding to 0.4 and 1.5 Li/MoS_3. The data for the sample charged to 0.4 Li/MoS_3 is represented by triangles while the data for the sample charged to 1.5 Li/MoS_3 is represented by squares. Representative error bars are shown in each spectrum. We have found that the depth profiling exhibits a uniform Li distribution up to a depth of about 18 μm (limit of our technique). The Li concentrations obtained by the NRA analysis for these

samples also agree quite well with the determination of the Li concentration from the accumulation of total charge density.

To determine the Li concentration by the nuclear reaction from the various samples, the γ-ray yields from the $^{7}Li(p,\gamma)^{8}Be$ reaction at an incident proton energy of 441 KeV were collected. Because of the resonance nature of this reaction, an incident proton beam of the right resonance energy would react with Li nuclei yielding the characteristic μ-rays. The front edges of Fig. 18, 19 and 20 are not the real Li distribution but appear due to the resonance beam reaction. The energy distribution of the proton beam gets wider (energy straggling) as the beam goes deeper into the samples, resulting a wider trailing edge of the Li distribution (in contrast with the sharp front edge). Even at the surface (front edge) the depth resolution is limited by the width of the resonance plus the intrinsic beam energy spread. The spectra shown in Figs. 18, 19 and 20 are therefore a convolution of the true distribution of Li and the beam spreading.

IV. ELECTROCHEMICAL MEASUREMENTS

A. Charging/Discharging measurements

We have charged/discharged several samples at different constant current densities. This is the first information available about the discharging behavior of pure a-MoS_3. In all previous cycling measurements a-MoS_3 power along with a binder was used as the active cathode. Another advantage of study thin film a-MoS_3 lies in the time scale. For a-MoS_3 powder pellets it requires several weeks to complete one charge/discharge cycle. On the other hand for thin film a-MoS_3 the cycling requires only several hours.

The measurement of the total charge density during charge-discharge cycling determfined the Li concentration in the a-MoS_3 thin films. This

secondary technique for the determination of Li concentration relies on the measurement of total charge accumulated during the cycling process and on the assumption of uniform distribution of Li in the active cathode material. We compared some of these results obtained by the secondary technique with primary analytical technique of NRA as discussed in the previous section.

Figures 21, 22 and 23 show the first cycle of ED-MoS_3(A) thin films cycled at 50$\mu A/cm^2$, 100$\mu A/cm^2$ and 500$\mu A/cm^2$ respectively. In each case, the cell voltage initially drops rapidly and then decreases gradually up to 3 Li/MoS_3 and again drops rapidly. The electrochemical performance of ED-MoS_3(A) and ED-MoS_3(NA) is similar.

In the charging/discharging process at low current densities the steps after insertion of 1 and 2 (Li/MoS_3 are clearly visible. However, as the current density increases the steps start to smear out.

B. Mechanism of Electrodeposition

In this section we report the results of a study of some of the electrochemical and chemical changes that take place during the electrodeposition reaction which we hope will lead to a better understanding of the mechanism of the electrodeposition of a-MoS_3.[4] The main analytical tools employed were Raman scattering and cyclic voltammetry. We find that the equilibrium between ATTM and a-MoS_3 is shifted to deposition of MoS_3 by the electrochemical oxidation of reduced sulfur to polysulfide.

1. Experimental details

The electrodeposition and electrochemical measurements were carried out with an IBM Instruments, EC/225-3a voltammetric analyzer. The electrodeposition bath consisted of a 0.04M ATTM solution in methanol or water. The color of both aqueous and non-aqueous solutions were dark brown.

The stability of the solutions were tested for 48 hrs. No precipitation or change in color were observed during and after this 48 hrs. time scale. The electrodeposition process was carried out at room temperature at various constant potentials, ranging from +0.3V to +1.5V (vs saturated calomel electrode (SCE) employing Pt as the working and counterelectrodes. In Refs. 4 and 5 the working electrode was glass slides coated with Sn-doped indium oxide (ITO) (nominal sheet resistance: 10 Ω/□, Nesatron glass from commerical sources), which allowed optical measurements to be performed. The working and counter electrodes for the cyclic voltammetry were platinum and the reference electrode was saturated calomel electrode (SCE). The pH was measured directly from the bath solutions.

Raman scattering was employed to characterize the various materials. Raman spectra were recorded at room temperature on a Spex model 1401/14018 double grating monochromator with a cooled photomultiplier tube (Products for Research, Inc. Model 9498-31). The backscattering geometry was used for all the measurements. The excitation light source was the 5245 Å line of an Ar-ion laser (Coherent Radiation CR-6, model 53 head).

The surface morphology was investigated by scanning electron microscopy (SEM), using a Hitachi Model 405A. Film thicknesses were measured by an Alpha-Step profiler (Tencor Instruments).

2. Experimental Results

The electrodeposited thin films were analyzed by Raman scattering spectroscopy. The thin films deposited both from aqueous and non-aqueous solutions in the potential range between +0.3V to 1.5V showed similar Raman spectra. In Fig. 1 we compare the Raman spectra, in the range 140-690 cm^{-1}, of a-MoS_3 prepared under various conditions. This has been discussed in Sec. III-A.

Figure 24 shows the SEM photographis of a representative ED-MoS_3(A) and ED-MoS_3(NA) thin films on ITO substrates at two different magnifications. The thickness of all the films was about 1 μm. The films are very smooth with many cracks. The ED-MoS_3 (NA) has more cracks in comparison with the ED-MoS_3(A) (for the same area). At lower magnification, the SEM photographs show that a typical crack width of ED-MoS_3(NA) is larger than the cracks found in ED-MoS_3(A) films, but the surface of the uncracked portion of the ED-MoS_3(NA) film was smoother in comparison with the ED-MoS_3(A) films. Magnification of the cracks suggests that they do not propagate all the way to reach the substrate.

The current-voltage curves observed by the cyclic voltammetry scans in an aqueous solution of ATTM (0.01 M, pH 7.5) are shown in Fig. 25. The current voltage curves shown in Fig. 26 were obtained from a non-aqueous (methanol) solution of ATTM (0.01 M, pH 8.5). Both Figs. 25 and 26 represent irreversible electrochemical reactions. The several, successive, cyclic voltammetry scans (a,b,c) shown in Figs. 25 and 26 were obtained at the same scan rate (100 mV/sec).Similar results were obtained at the slower scan rates. The cyclic voltammetric scans were initiated with an acid (HNO_3:HCl) cleaned platinum working electrode; several scans were recorded for the same electrode. The anodic current density decreases with the repetition of the cyclic voltammetry scan at the same working electrode as shown in Figs. 25 and 26. After cycling, deposited material on the working electrode was observed. These deposits were later identified as a-MoS_3 by the Raman studies. The decrease of the anodic current density can be explained in terms of the deposition of high resistivity a-MoS_3 thin film on the working platinum electrode, generated from the irreversible electrochemical reaction. The oxidation peaks from the non-aqueous and aqueous solution appear around 0.55

V. The slight difference in the oxidation peaks from the two solutions is due mainly to the larger IR drop in the non-aqueous electrolyte.

3. Discussion of Results

The results show that the deposition of a-MoS_3 thin films is driven electrochemically yet there is no change in the apparent net charge of the molybdenum or sulfur in both ATTM and MoS_3. Molybdenum trisulfide is known to be solube in $(NH_4)_2S$ to form ATTM. The film deposition is the reverse of the dissolution reaction. Both reactions can be represented as:

$$MoS_3(s) + (NH_4)^+(sol) + S^{2-} \leftrightarrow NH_4^+(sol) + (MoS_4)^{2-}(sol) \quad (9)$$

The formal valence of the sulfur and the molybdenum do not change in the reaction. The thermal decomposition of ATTM to MoS_3 powder starts at about 200°C. There is no deposition of MoS_3 from either the aqueous (pH 7.5) or non-aqueous (pH 8.5) solutions of ATTM, at room temperature, under open circuit condition. The Raman spectra show that the electrodeposited films and the thermally deposited pellet are similar, as discussed above.

The first issue is to determine the nature of the oxidation peak which appears around 0.55 V vs. SCE and is responsible for facilitating the electrodeposition reaction as discussed above. This was accomplished by depleting the starting solution of 0.01M ATTM by depositing as many as possible a-MoS_3 thin films on a series of PT working electrodes, until there was no additional film deposition on a fresh electrode. We designate the residue solution which was obtained from the deposition bath after complete depletion of MoS_3 as R-solution.

Figure 27 shows the cyclic voltammogram of the R-solution (dashed line) and the cyclic voltammetry obtained from a standard polysulfide (.01/.01/.01M, Na_2S/NaOH/S solution (solid line) at 100 mV/Sec scan rate. The cyclic

voltammograms of both the R-solution and the polysulfide solution are irreversible and agree quite well with each other. The major difference between the two is the current density which is most likely due to the different concentrations of the polysulfide in the two solutions.

Figure 28 shows the Raman spectra of the R-solution (dotted line) (the spectra are similar for both the aqueous and non-aqueous solutions), the Raman spectra of 0.01:0.01:0.01 polysulfide solution (dashed line) and also fresh 0.01 M ATTM solution (solid line) again the spectra are similar for both the aqueous and non-aqueous solutions), at the laser power density of 60 mW/cm^2. Due to the similarity of the Raman spectra of the polysulfide solution with the ATTM solution, we cannot make a definitive statement from this Raman study. The Raman band around 470 cm^{-1} observed in all the solutions mentioned above could be due S-S stretching mode corresponding to open chain polysulfide. However, assuming the removal of all the MoS_3 from the ATTM solution, these spectra add to the accumulating evidence that principal component in the R-solution is polysulfide.

During the preparation of the R-solution, particularly in the non-aqueous electrolyte, a yellow deposit was visible on the walls of the electrochemical cell and on the counter electrode which was left unchanged during the repeated depositions of the MoS_3 films. Figure 29 shows the Raman spectrum of this deposit (solid line) together with the spectrum of elemental sulfur (dotted line). The main features of the two spectra are identical. Seven peaks centered at 85±2 cm^{-1}, 154±2 cm^{-1}, 186±2 cm^{-1}, 218±2 cm^{-1}, 246±2 cm^{-1}, 436±2 cm^{-1} and 472±2 cm^{-1} can be seen. The basic features of the spectra and the peak positions agree with the assignment of Scott et.al to a molecular unit S_8 of D_{4d} symmetry. Thus, we identify this deposit as elemental sulfur.

These results show clearly that oxidation of sulfide to polysulfide takes place during the deposition of MoS_3 from ATTM under our experimental conditions. The most straightforward explanation is the shift of the equilibrium in the reaction of Eq. (9) to the left by removal of sulfur from ATTM by oxidation to form polysulfide. More subtle explanations such as a change in local pH or change in the dielectric properties of the interface are also possible considering that an external voltage is not required for the deposition of MoS_3 from ATTM in acidic media. Additional experimental work is needed to clarify the possible role of these other mechanisms.

The formation of polysulfide suggests that the anodic reaction takes the following form:

$$x(MoS_4)^{2-} \rightarrow xMoS_3 + (S_x)^{2-} + 2(x - 1)e^- \qquad (10)$$

leading to the deposition of MoS_3 while the polysulfide is dissolved in the electrolyte and eventually diffuses to the counter electrode to be reduced back to sulfide. We did not follow the potential of the counter electrode during the deposition process and as a result, were unable to determine the nature of the reductive process that initially takes place on the counter electrode. Reduction of oxygen is a possibility. The amount of sulfur that was found in the R solution strongly suggests that the reduction of the polysulfide is not very efficient.

It is also possible that some of the sulfur is incorporated into the film but the agreement between the Raman spectra of the thermally decomposed MoS_3 powder and the electrodeposited thin films tends to exclude this possibility.

Although the deposition itself is not a faradaic process, one can define the faradaic efficiency as the molar ratio of the deposited MoS_3 and the

charge that flows through the system. At the initial stages of deposition this ratio reaches 0.95, which tends to indicate quantitative formation of polysulfide.

C. Impedance Measurements

We have performed frequency dependent studies of the real and imaginary parts of the complex impedance.[22] The measurements were made in 1M KCl in the range $0.01\text{-}10^5$Hz using a Solartron 1250 Frequency Response Analyzer. We investigated the impedance spectra of several samples of different eleectrode potentials ranging from -1V to -0.3V. Figures 30, 31, 32 and 33 display the impedance spectra of a-MoS_3(A) deposited at 0.3V, a-MoS_3(A) deposited at 1.5V, a-MoS_3(NA) deposited at 0.3V and a-MoS_3(NA) deposited at 1.5V, respectively. The electrode potential was -0.35V in all cases. The thickness and area of the samples was 1μm and 0.04 cm^2, respectively.

The capacitance of the samples can be deduced from the high frequency behavior of the imaginary component of the impedance. For all our samples we find a capacitance of order 1μf. However, based on an estimate of the dielectric constant of the material ($\varepsilon \approx 10$) and from the physical dimensions of the sample (thickness ≈ 1μm and area ≈ 0.04 cm^2) we deduce a capacitance of about 10^{-4} μf. This is four orders of magnitude smaller than the boserved capacitance. At the present we have no explanation for this phenomenon.

V. REFERENCES

1. A.J. Jacobson, R.R. Chianelli, S.M. Rich and M.W. Whittingham, Mat. Res. Bull. 14, 1437 (1979).

2. A.J. Jacobson, Solid State Ionics 5, 65 (1981).

3. R.N. Bhattacharya, C.Y. Lee, F.H. Pollak and D.M. Schleich, Disordered Semiconductors, ed. by M.A. Kastner, G.A. Thomas and S.R. Ovshinsky (Plenum, New York, 1987) p. 247; also, J. Non-Crystalline Solids 91, 235 (1987).

4. R.N. Bhattacharya, F.H. Pollak, M. Tomkiewicz and D.M. Schleich, submitted to Mat. Res. Bull.

5. Biltz Kocher, Z. Anorg. Chem. 148, 72 (1941).

6. J.C. Wildervanck and F. Jennilek, Z. Anorg. Allg. Chem. 328, 309 (1964); K. Blitz Z. Anorg. Allgem. 148, 72 (1941).

7. J.J. Auborn, Y.L. Barberio, K.J. Hanson, D.M. Schleich and M.J. Martin, J. Electrochem. Soc. 134, 580 (1987).

8. See, for example, C.H. Chang and S.S. Chan, J. Catalysis 72, 139 (1981) and references therein.

9. See, for example, F.Z. Chien, S.C. Moss, K.S. Liang and R.R. Chianelli, Phys. Rev. B29, 4606 (1984) and references therein.

10. See, for example, F.H. Pollak and R. Tsu in Proceedings of the Society of Photo-Optical Instrumentation Engineers, (SPIE, Bellingham, 1984) 452, 26 (1984).

11. J.N. Gan, T. Tauc, V.G. Lambrecht, Jr., and M. Robbins, Phys. Rev. B12, 5797 (1975).

12. J. Tauc, R. Grigorovici and A. Vancu, Phys. Status Solidi 15, 627 (1966).

13. C.D. Cody, T. Tiedje, B. Abeles, B. Brooks and Y. Goldstein, Phys. Rev. Letts, 47, 1480 (1981).

14. J. Melsheimer and D. Ziegler, Thin Solid Films, 129, 35 (1985).

15. See, for example, F.H. Pollak in Proceedings of the Society of Photo-Optical Instrumentation Engineers, (SPIE, Bellingham, 1981) 276, 142 (1981); D.E. Aspnes in Handbook on Semiconductors, ed. by T.S. Moss (North Holland, New York, 1980), Vol. 2. p. 109.

16. H. Okamoto, T. Yamaguchi and Y. Hamakawa, Solar Energy Mat. 2, 313 (1980).

17. Y. Hamakawa in Semiconductors and Semimetals, Vol. 21B, edited by J.I. Pankove, (Academic Press, New York 1984). p.

18. See, for example, R.V. Kasowski, Phys. Rev. Lett., 30, 1175 (1973) and references therein.

19. J.W. Mayer and E. Rimini, Ion Beam Handbook for Materials Analysis, (Academic Press, New York, 1977) and references therein.

20. R.N. Bhattacharya, D. Yan, P.M.S. Lesser, F.H. Pollak and D.M. Schleich, Proceedings of the Symposium on Primary and Secondary Ambient Temperature Lithium Batteries, ed. by J.P. Gabano, Z. Takehara and P. Bro (Electrochemical Society, Princeton, 1988) Vol. 88-6, p. 443.

21. J.B. Marion and F.C. Young, Nuclear Reaction Analysis, Graphs and Tables (North Holland, Amsterdam, 1968).

22. M. Tomkiewicz, J. Electrochem. Soc. 126, 1505 (1979); also, J. Electrochem. Soc. 127, 1517 (1980); also, Surf. Sci. 101, 186 (1980).

VI. FIGURE CAPTIONS

1. Raman spectra at 300K of ED-MoS_3 (NA) sample (solid line), an ED-MoS_3 (A) sample (dotted line) and a TD-MoS_3 sample (dashed line) using the 5145 A line of an Ar-ion laser.
2. Raman spectra at 300K of c-MoS_2 (dotted line) and μc-MoS_2 (dashed line) using the 5145 A line of an ar-ion laser.
3. Transmission spectra of two ED-MoS_3 (NA) samples with thickness of 0.18 μm (dotted line and 0.63 μm (dashed line).
4. Square root of the product of the absorption coefficient and photon energy vs photon energy for ED-MoS_3 (NA) (solid line) and Ed-MoS_3 (A) (dotted line). The dashed line represents a linear fit. Representative error bars for $(\alpha\hbar\omega)^{1/2}$ are shown.
5. Electrolyte electroreflectance spectrum at 300 K of an ED-MoS_3 (NA) sample (solid line) and on ED-MoS_3 (A) sample (dotted line). Shown by arrows are the fundamental gap as deduced from the absorption measurements of Fig. 4.
6. Electrolyte electroreflectance spectrum at 300K of c-MoS_2.
7. Electrolyte electroreflectance spectrum at 300K of μc-MoS_2.
8. The typical Li insertion (discharging) curve of an electrodeposited a-MoS_3 thin film at 100 $\mu A/cm^2$ constant current density.
9. The schematic diagram of the scattering chamber for Nuclear Reaction Analysis.
10. The Rutherford backscattering spectrum of an electrodeposited a-MoS_3 thin film on a Ni substrate (E_o = 460 KeV).
11. The Rutherford backscattering spectrum of an electrodeposited a-MoS_3

thin film on a ITO substrate (E_o = 480 KeV).

12. The Rutherford backscattering spectrum of TD-MoS_3 (E_o = 455 KeV).

13. The Rutherford backscattering spectrum of the LiF standard sample (E_o = 465 KeV).

14. The Rutherford backscattering spectrum of the LiCl standard sample (E_o = 425 KeV).

15. A typical γ-ray spectrum from the reaction $^7Li(p,\gamma)^8Be$ at the 441 KeV resonance proton energy.

16. The energy dependence of the stopping power of MoS_3Li_x, assuming a constant density of MoS_3 for various x.

17. The depth scale in angstrom vs the incident proton beam energy.

18. The absolute Li concentration vs depth of a ED-MoS_3 (NA) sample deposited on a Ni substrate.

19. The absolute Li concentration vs depth of a ED-MoS_3 (NA) sample deposited on an ITO substrate.

20. The absolute Li concentration vs depth of a TD-MoS_3 sample. Δ corresponds to 0.4 Li/MoS_3, corresponds to 1.5 Li/MoS_3.

21. First cycle of the charge/discharge process of a ED-MoS_3(A) film (deposited at + 0.3V) at a current density of 50 $\mu A/cm^2$.

22. First cycle of the charge/discharge process of a ED-MoS_3(A) film (deposited at + 0.3V) at a current density of 100 $\mu A/cm^2$.

23. First cycle of the charge/discharge process of a ED-MoS_3(A) film (deposited at + 0.3V) at a current density of 500 $\mu A/cm^2$.

24. (a) SEM photograph of ED-MoS_3(NA) thin film on Nesatron, solid line represents 150 μm; (b) SEM photograph of ED-MoS_3 (NA) thin film on Nesatron, solid line represents 2 μm; (c) SEM photograph of ED-MoS_3(A) thin film on Nesatron, solid line represents 150 μm; (d) SEM photograph

of ED-MoS_3 (A) thin film on Nesatron, solid line represents 2 μm.

25. Cyclic voltammogram (scan rate 100 mV/sec) of an aqueous solution of ATTM (0.01M). (a) Solid line-1st scan; (b) dashed line-2nd scan; c. dotted line-3rd scan. (surface area = 0.04 cm^2).

26. Cyclic voltammogram of a non-aqueous solution of ATTM (0.01 M). (a) Solid line-1st scan; (b) dashed line-2nd scan; (c) dotted line-3rd scan. The same conditions as in figure 25.

27. Cyclic voltammogram of the R-solution (dashed line) and of a (.01/.01/.01M, Na_2S/ NaOH/S) polysulfide solution (solid line). (scan rate 100 mV/sec.

28. Raman spectra at 300K of the polysulfide solution (same composition as in figure 27) (dashed line), both aqueous and non-aqueous ATTM solution (solid line) and R-solutions (dotted line) using the 5145 Å line of an Ar-ion laser.

29. Raman spectra at 300°K of standard sulfur (dotted line) and the deposited sulfur from ATTM solution (solid line) using the 5145 Å line of an Ar-ion laser.

30. Real and imaginary components of the complex impedance as a function of frequency of a-MoS_3(A) deposited at 0.3V.

31. Real and imaginary components of the complex impedance as a function of frequency of a-MoS_3(A) deposited at 1.5V.

32. Real and imaginary components of the complex impedance as a function of frequency of a-MoS_3(NA) deposited at 0.3V.

33. Real and imaginary components of the complex impedance as a function of frequency of a-MoS_3(NA) deposited at 1.5V.

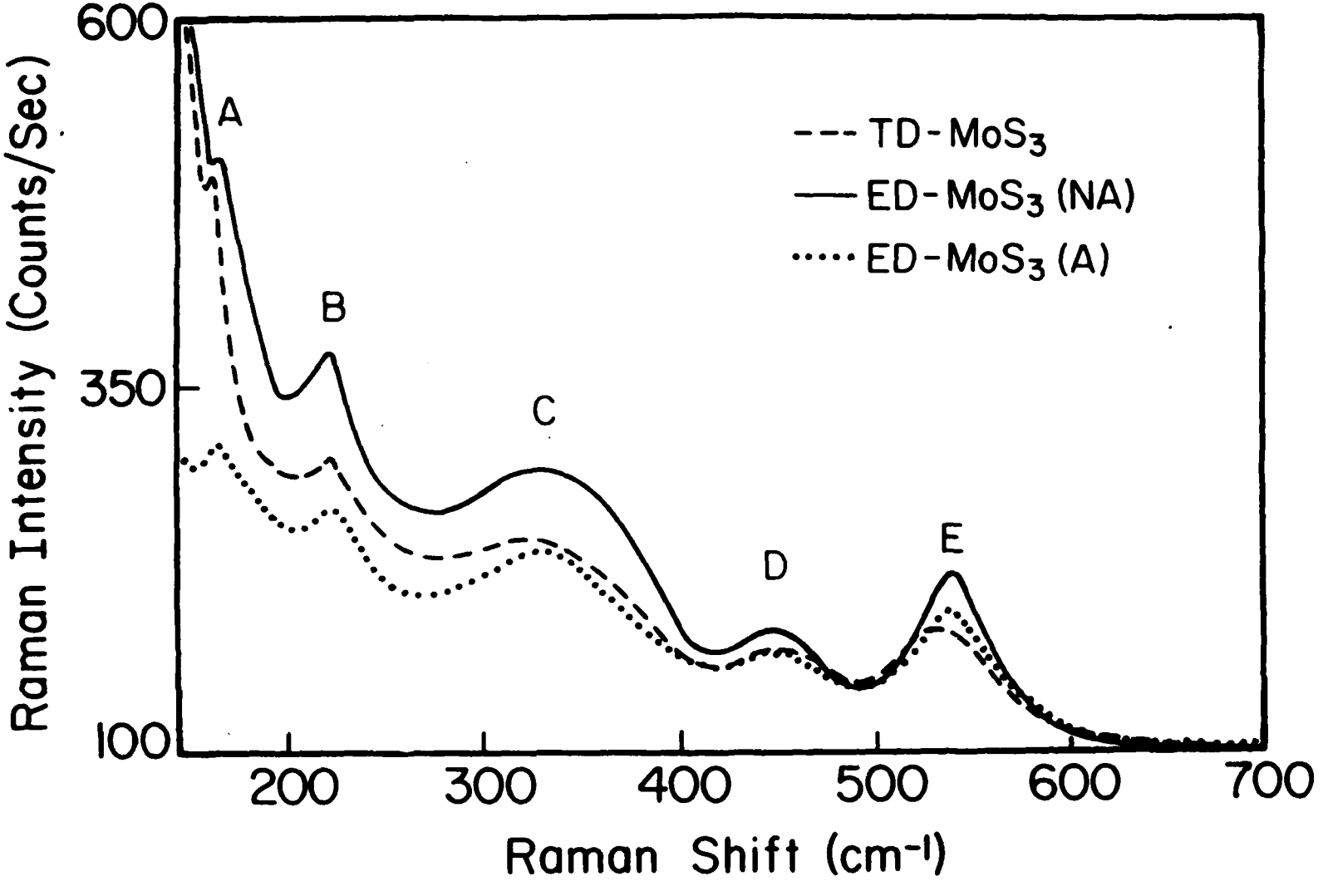
600
350
100
Raman Intensity (Counts/Sec)
A
B
C
D
E
--- TD-MoS3
—— ED-MoS3 (NA)
····· ED-MoS3 (A)
200
300
400
500
600
700
Raman Shift (cm-1)

Fig. 1

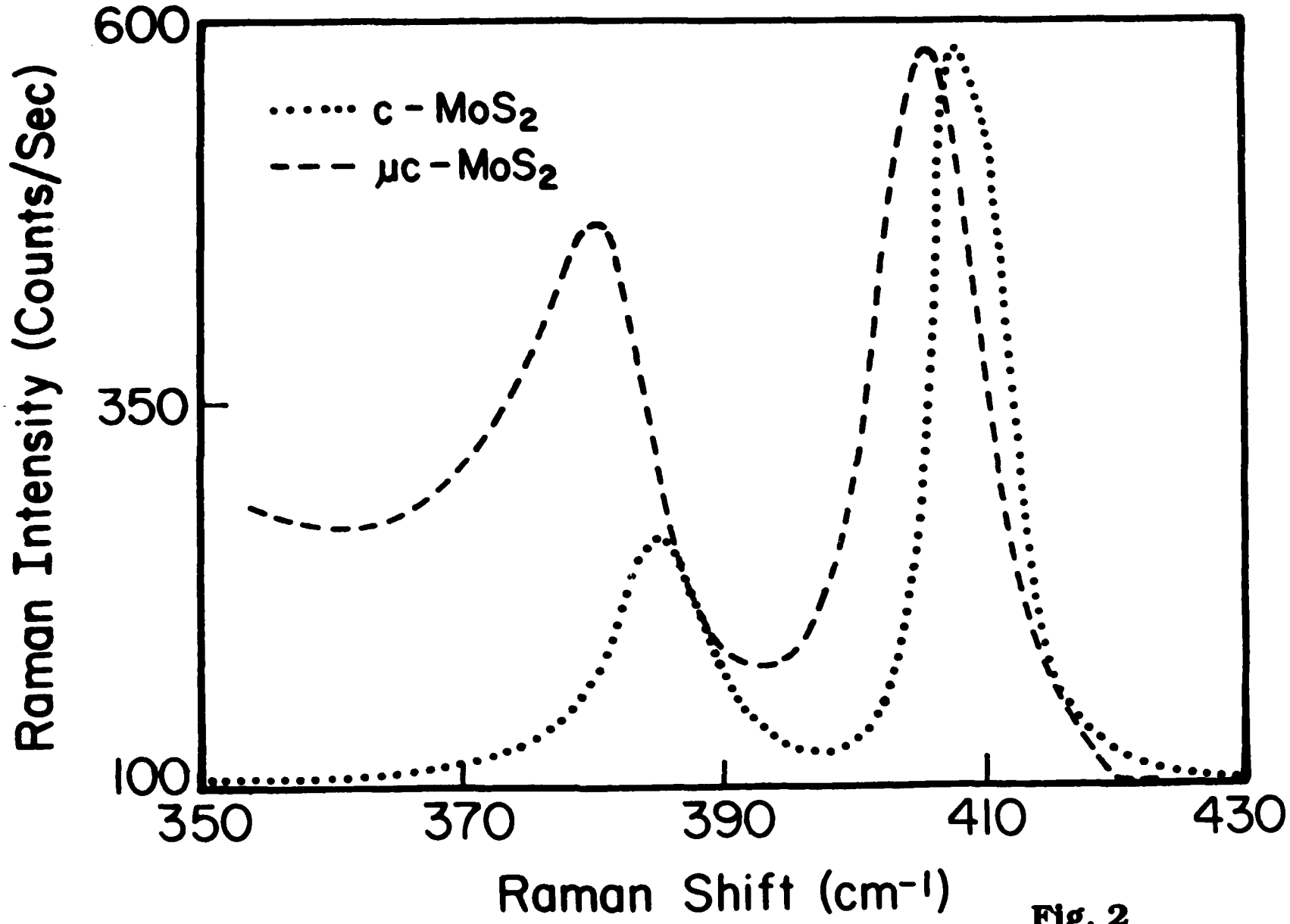
600
350
100
Raman Intensity (Counts/Sec)
..... c - MoS2
--- μc - MoS2
350
370
390
410
430
Raman Shift (cm-1)

Fig. 2

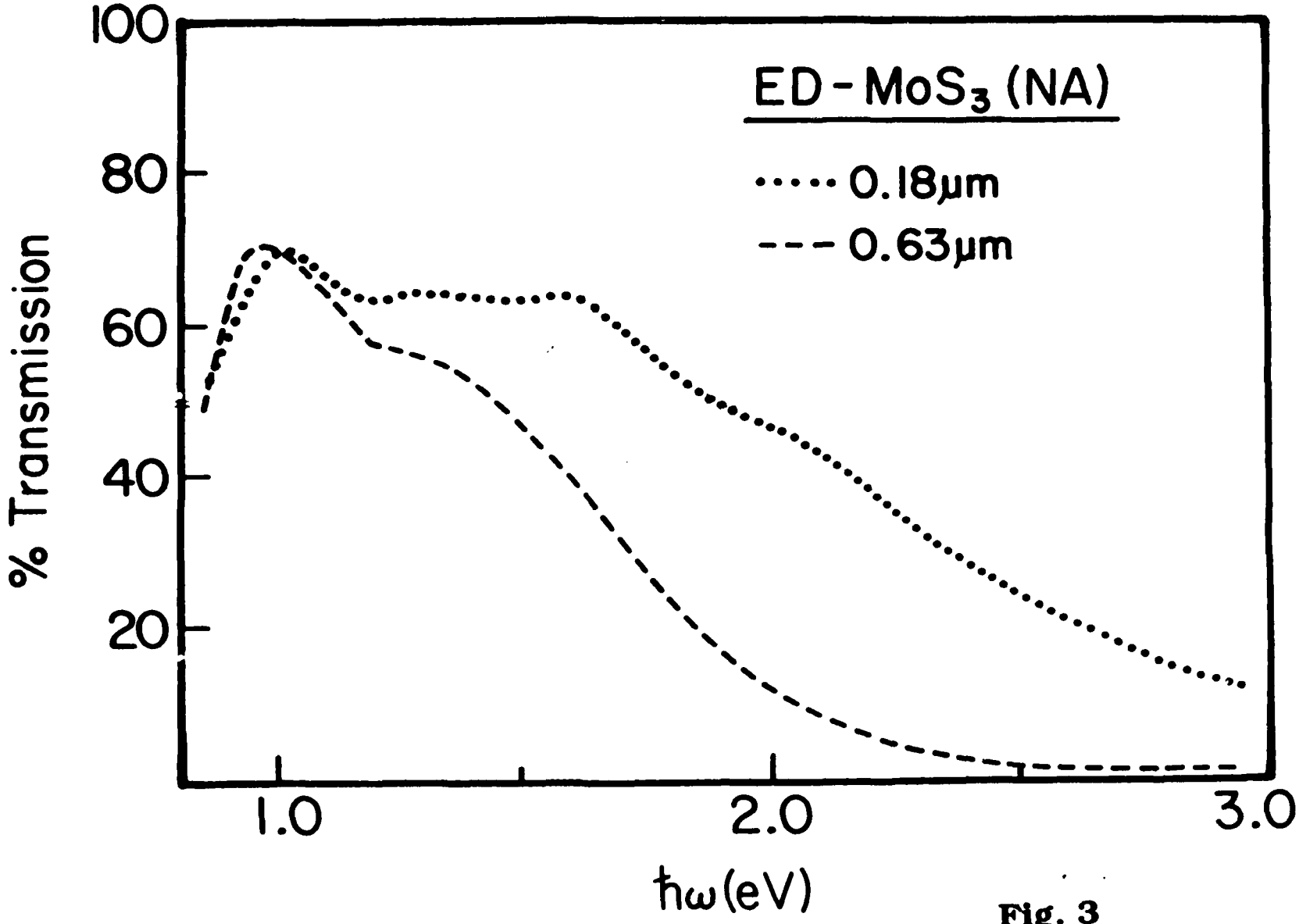
ED - MoS3 (NA)
0.18μm
0.63μm
% Transmission
100
80
60
40
20
1.0
2.0
3.0
ħω(eV)

Fig. 3

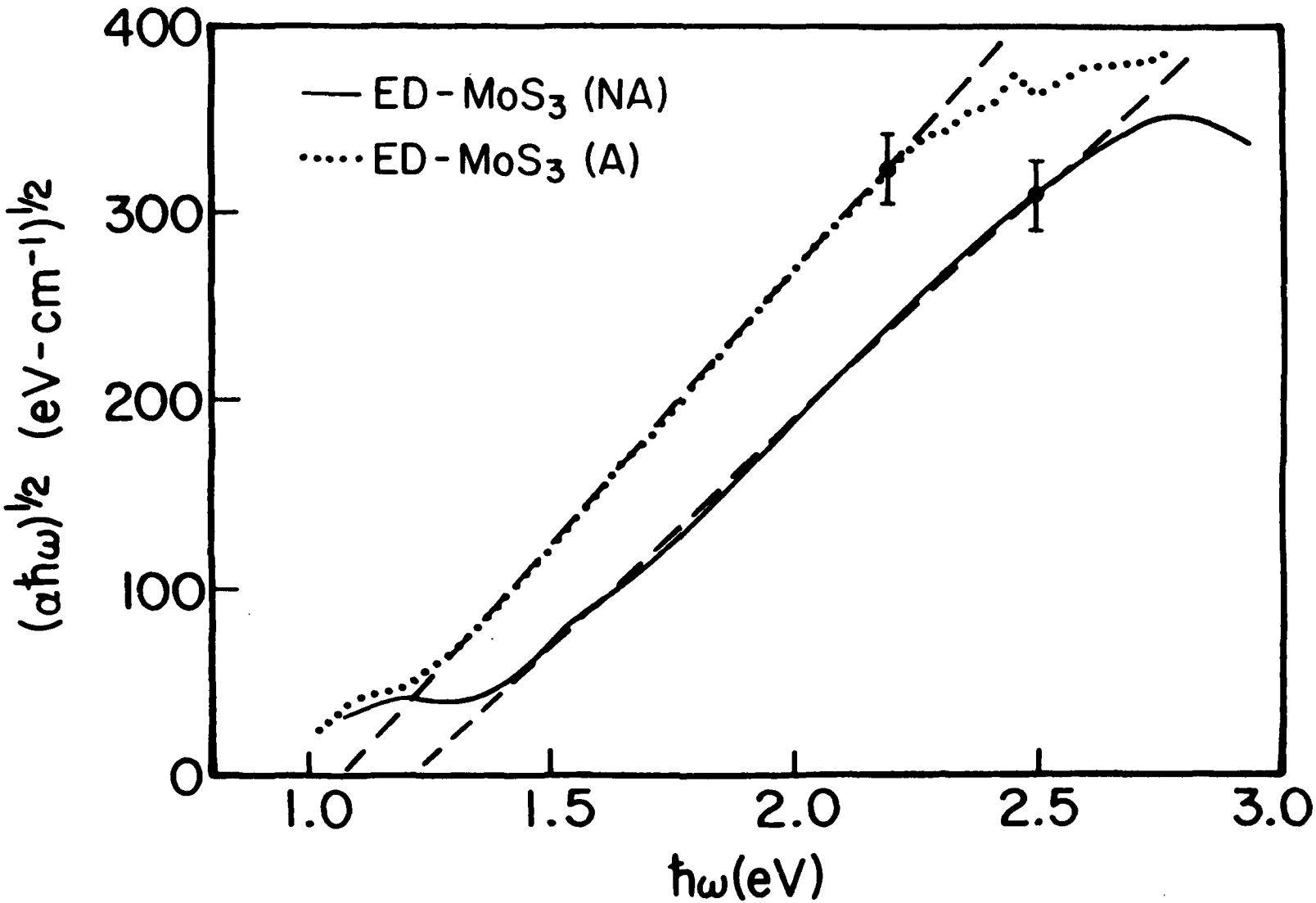
400
300
200
100
0
— ED - MoS3 (NA)
····· ED - MoS3 (A)
(αħω)^1/2 (eV-cm^-1)^1/2
1.0
1.5
2.0
2.5
3.0
ħω(eV)

Fig. 4

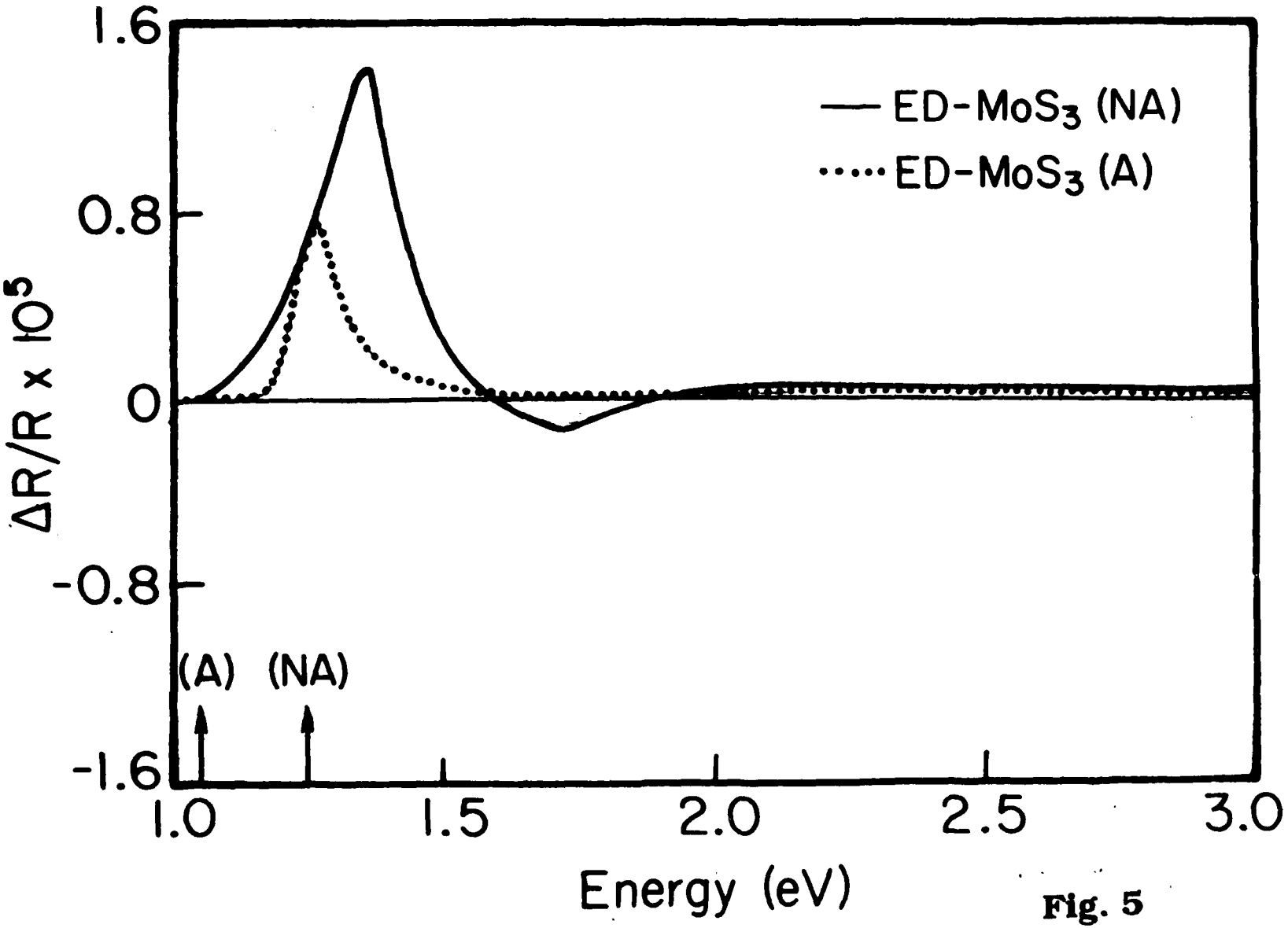
1.6
0.8
0
-0.8
-1.6
ΔR/R x 10⁵
— ED-MoS₃ (NA)
····· ED-MoS₃ (A)
(A)
(NA)
1.0
1.5
2.0
2.5
3.0
Energy (eV)

Fig. 5

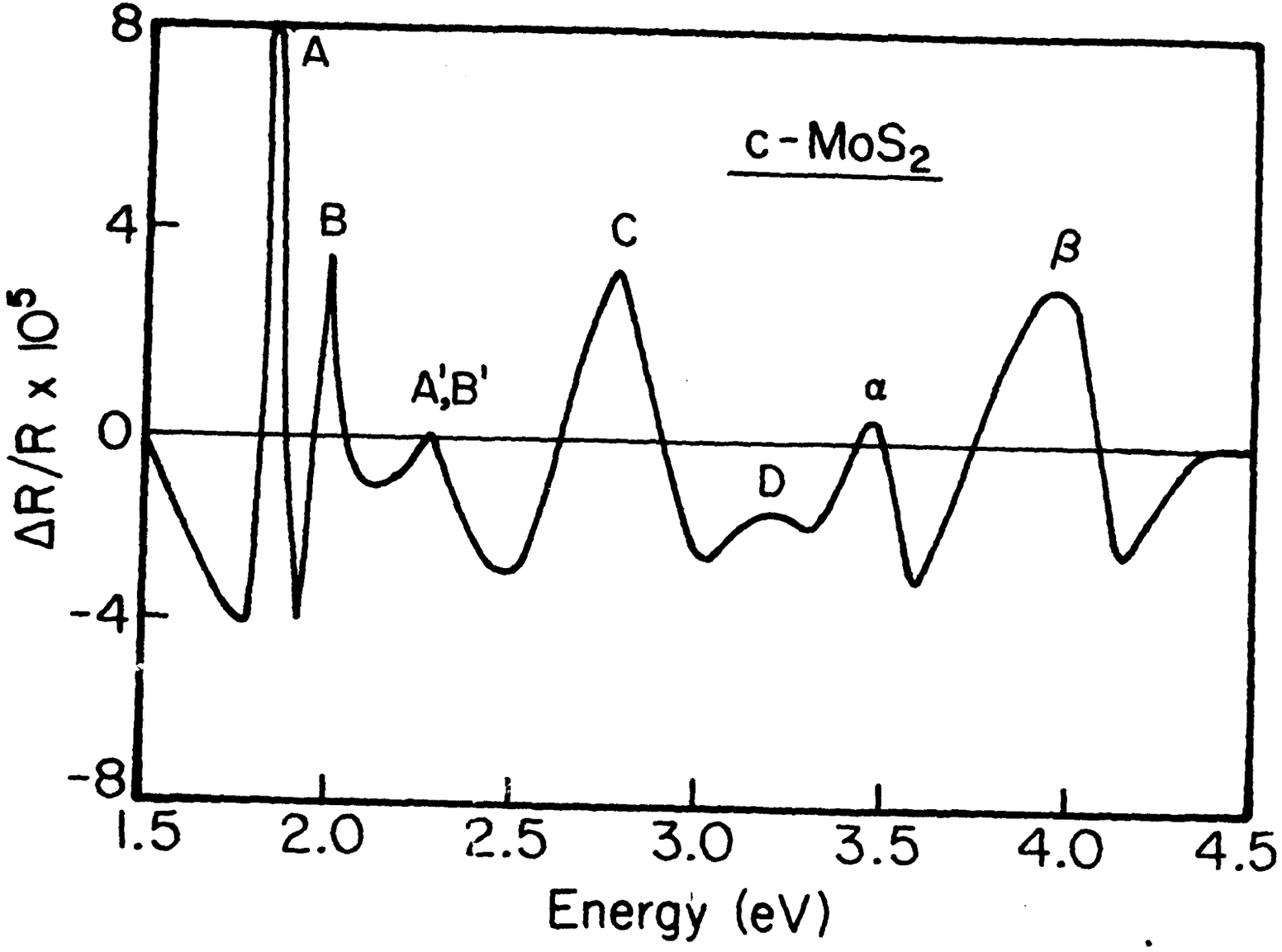

Fig. 6

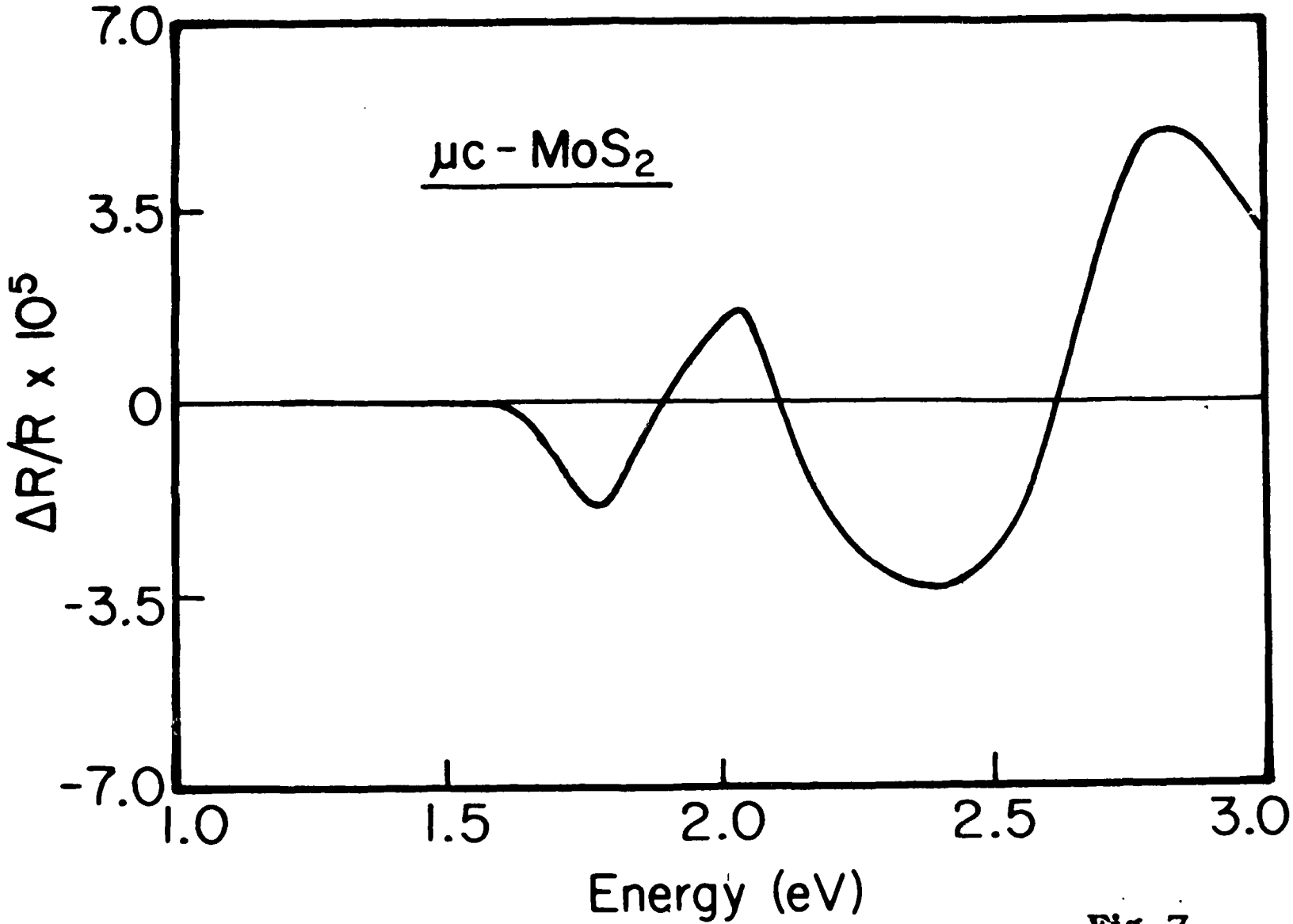

Fig. 7

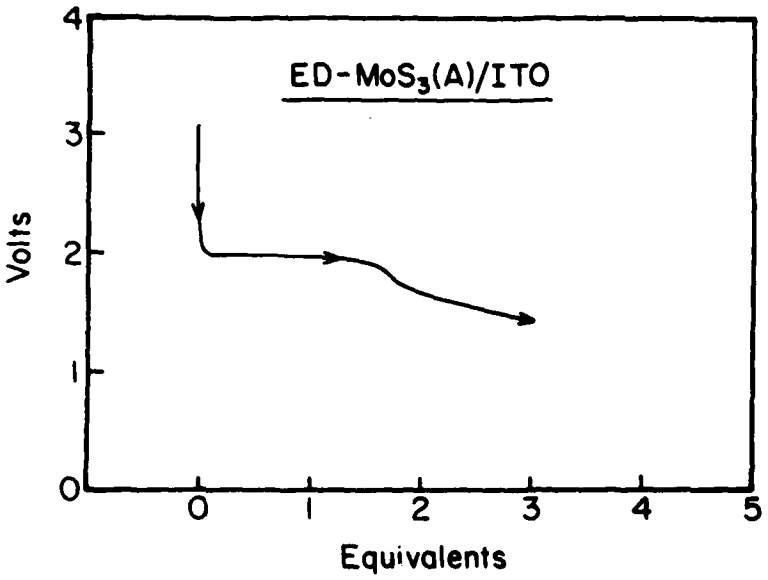
ED-MoS3(A)/ITO
Volts
Equivalents
0
1
2
3
4
5

Fig. 8

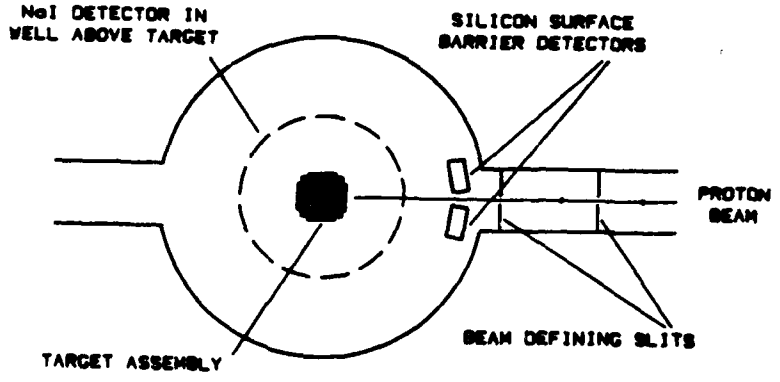
NaI DETECTOR IN WELL ABOVE TARGET
SILICON SURFACE BARRIER DETECTORS
PROTON BEAM
BEAM DEFINING SLITS
TARGET ASSEMBLY

Fig. 9

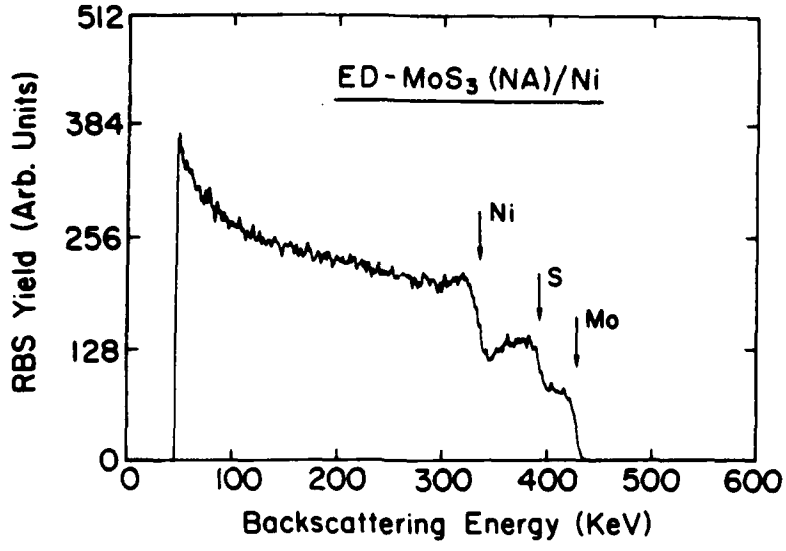
512
384
256
128
0
RBS Yield (Arb. Units)
ED-MoS3 (NA)/Ni
Ni
S
Mo
0
100
200
300
400
500
600
Backscattering Energy (KeV)

Fig. 10

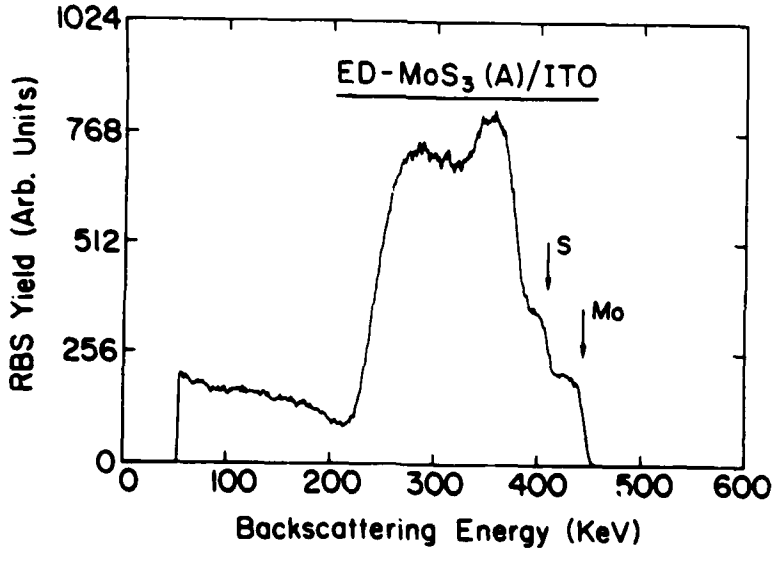
1024
768
512
256
0
RBS Yield (Arb. Units)
ED-MoS3 (A)/ITO
S
Mo
0
100
200
300
400
500
600
Backscattering Energy (KeV)

Fig. 11

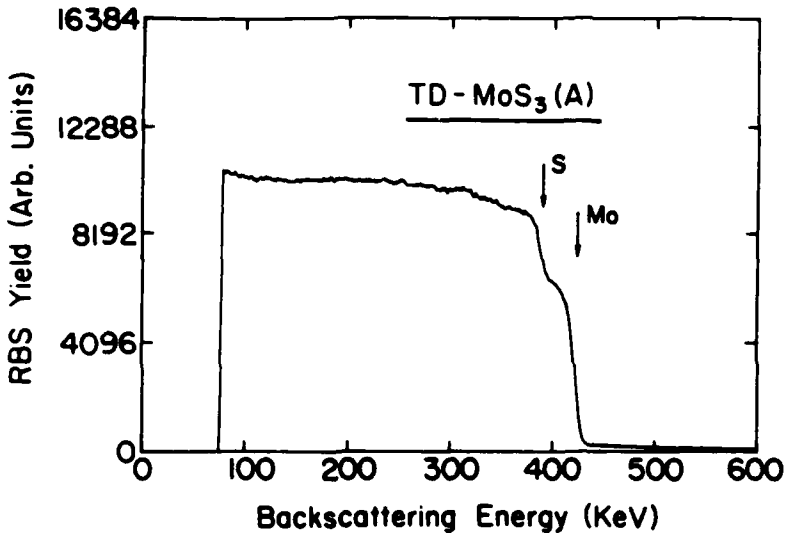
16384
12288
8192
4096
0
RBS Yield (Arb. Units)
TD - MoS3 (A)
S
Mo
0
100
200
300
400
500
600
Backscattering Energy (KeV)

Fig. 12

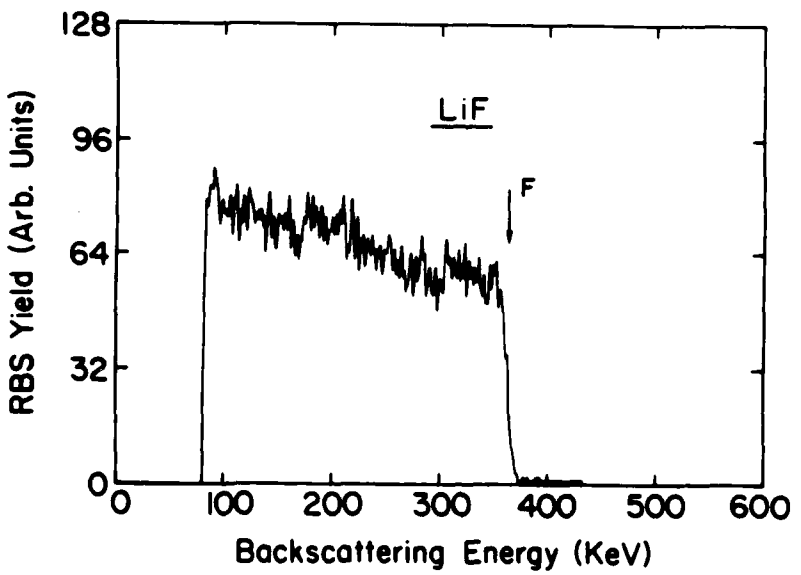
128
96
64
32
0
RBS Yield (Arb. Units)
LiF
F
0
100
200
300
400
500
600
Backscattering Energy (KeV)

Fig. 13

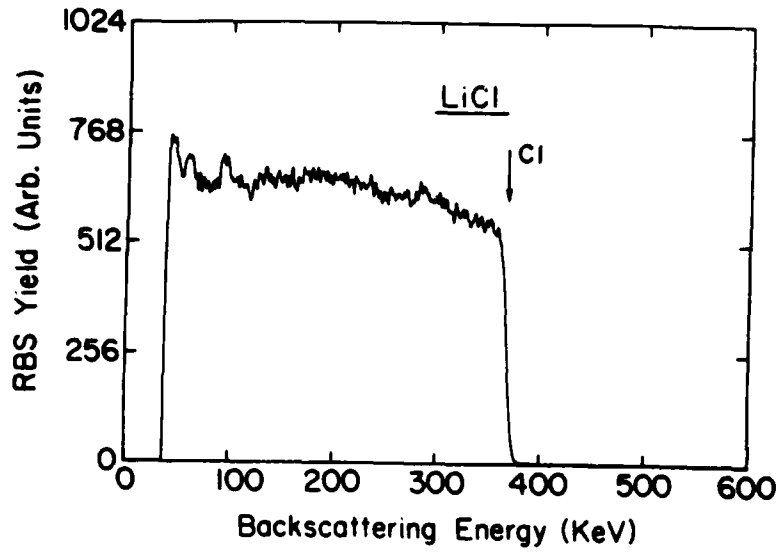
1024
768
512
256
0
RBS Yield (Arb. Units)
LiCl
Cl
0
100
200
300
400
500
600
Backscattering Energy (KeV)

Fig. 14

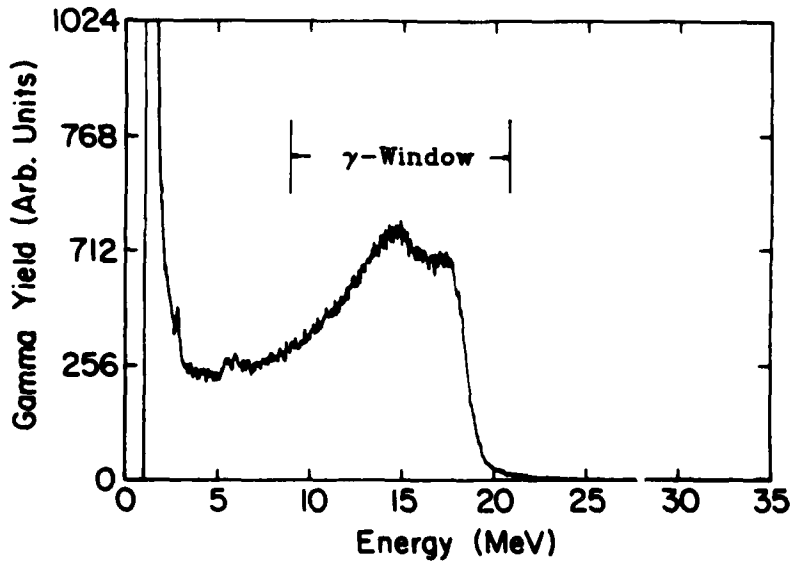
1024
768
712
256
0
Gamma Yield (Arb. Units)
γ-Window
0
5
10
15
20
25
30
35
Energy (MeV)

Fig. 15

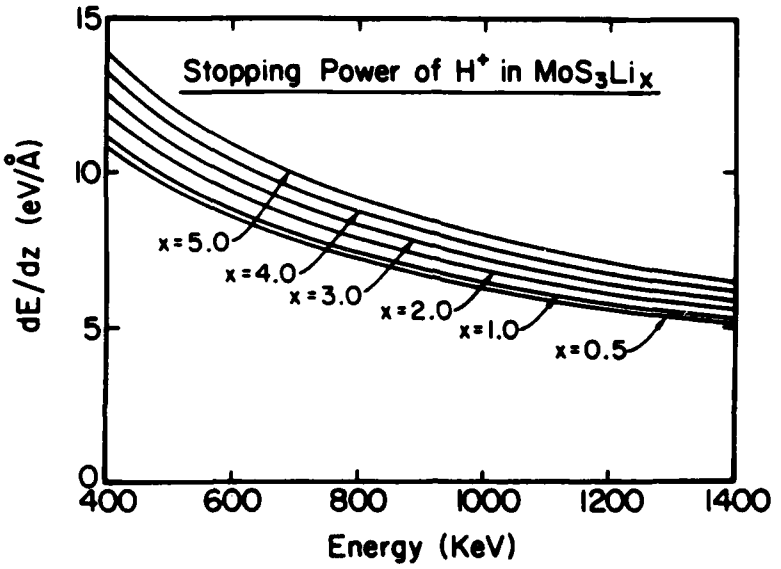
Stopping Power of H+ in MoS3Lix
dE/dz (eV/Å)
15
10
5
0
x=5.0
x=4.0
x=3.0
x=2.0
x=1.0
x=0.5
400
600
800
1000
1200
1400
Energy (KeV)

Fig. 16

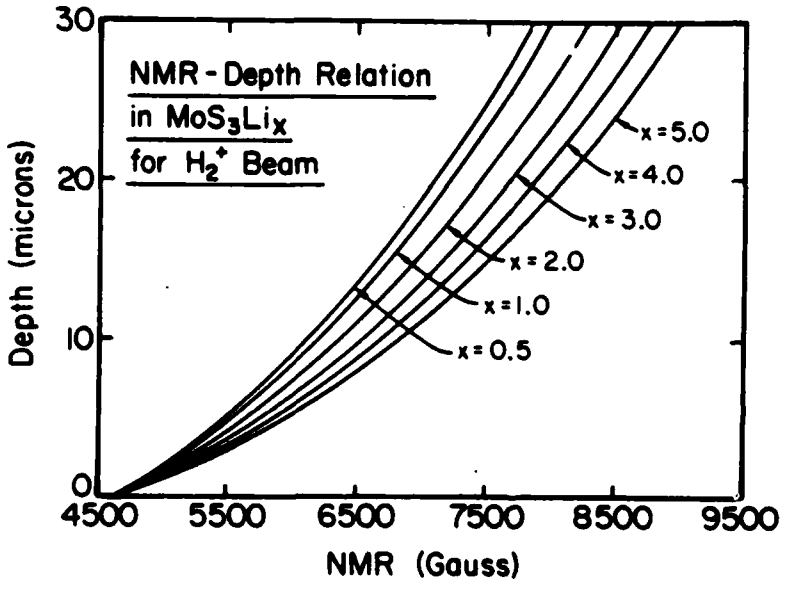
NMR - Depth Relation
in MoS3Lix
for H2+ Beam
Depth (microns)
30
20
10
0
x=5.0
x=4.0
x=3.0
x=2.0
x=1.0
x=0.5
4500
5500
6500
7500
8500
9500
NMR (Gauss)

Fig. 17

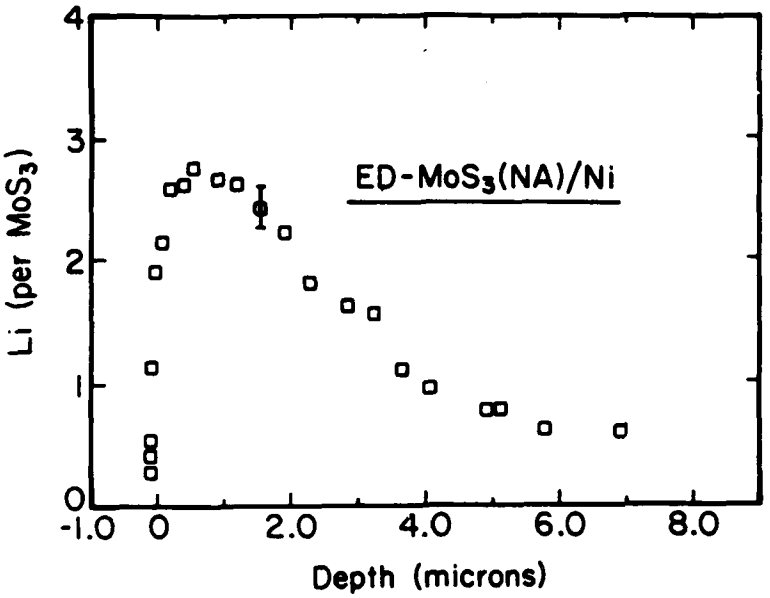
ED-MoS3(NA)/Ni
Li (per MoS3)
Depth (microns)
0
1
2
3
4
-1.0
0
2.0
4.0
6.0
8.0

Fig. 18

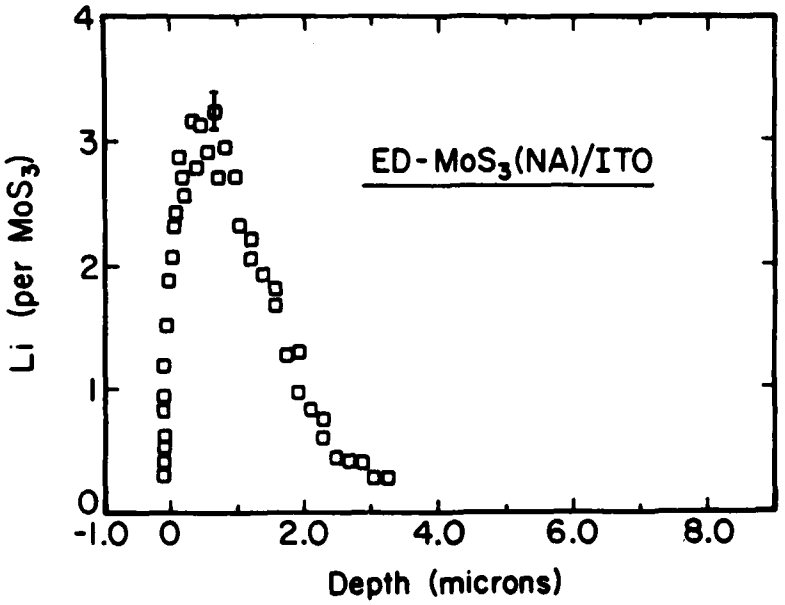
ED-MoS3(NA)/ITO
Li (per MoS3)
Depth (microns)
0
1
2
3
4
-1.0
0
2.0
4.0
6.0
8.0

Fig. 19

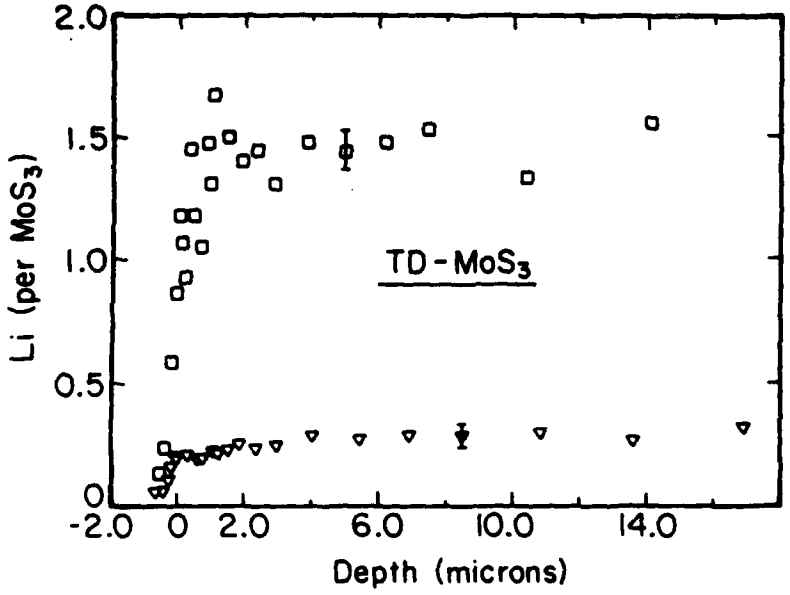

Fig. 20

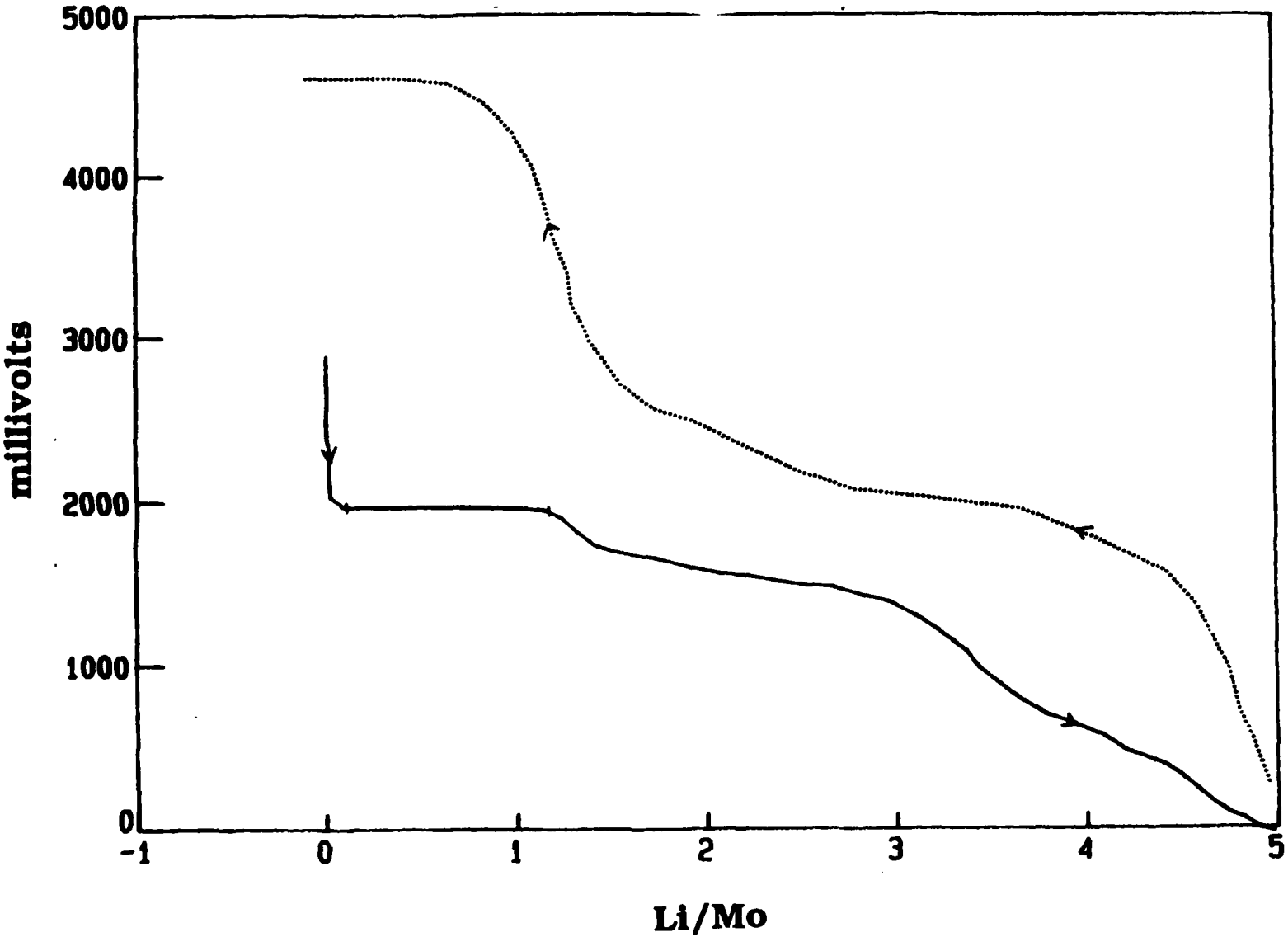

Fig. 21

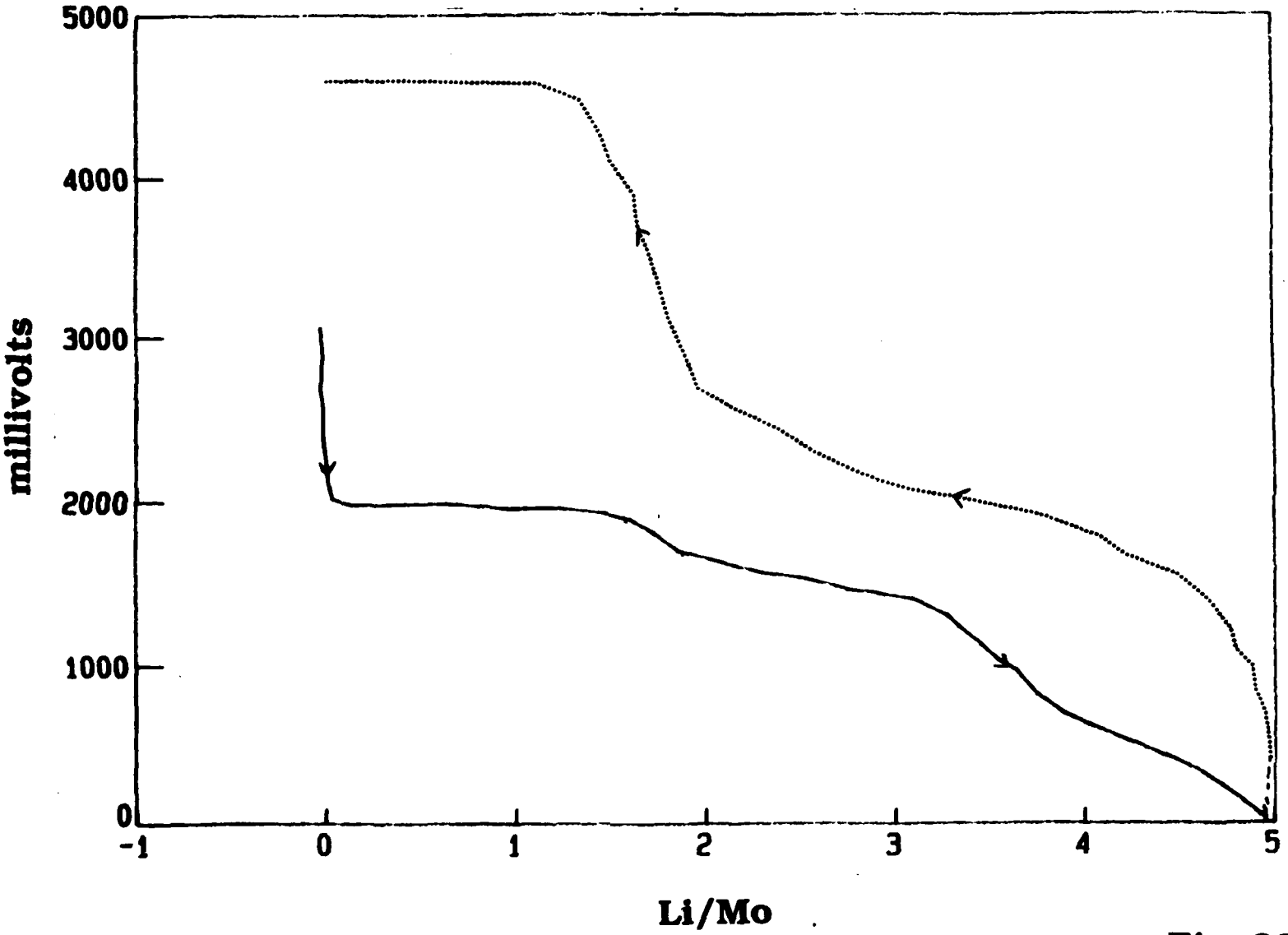

Fig. 22

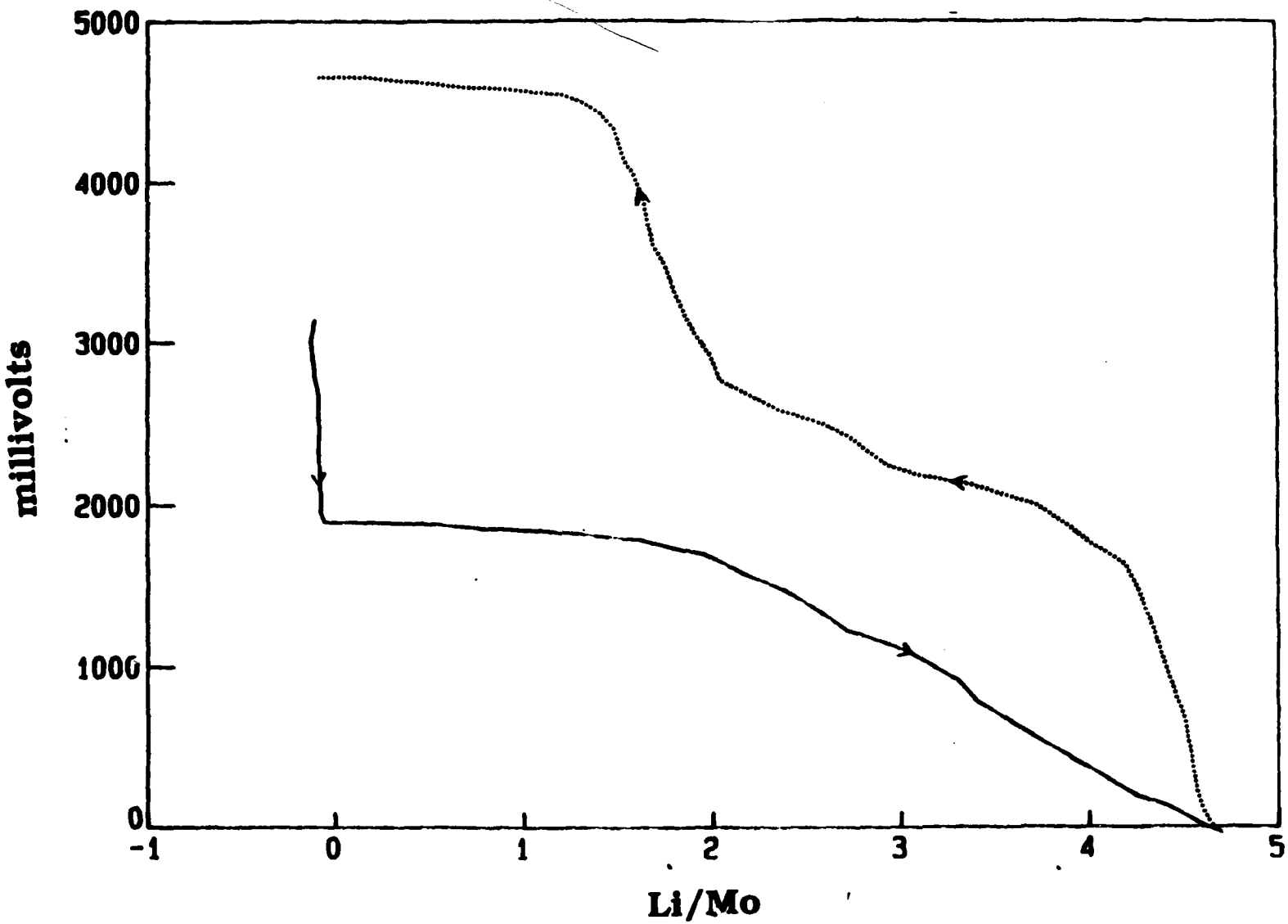

Fig. 23

(a) ED-MoS_3(NA)

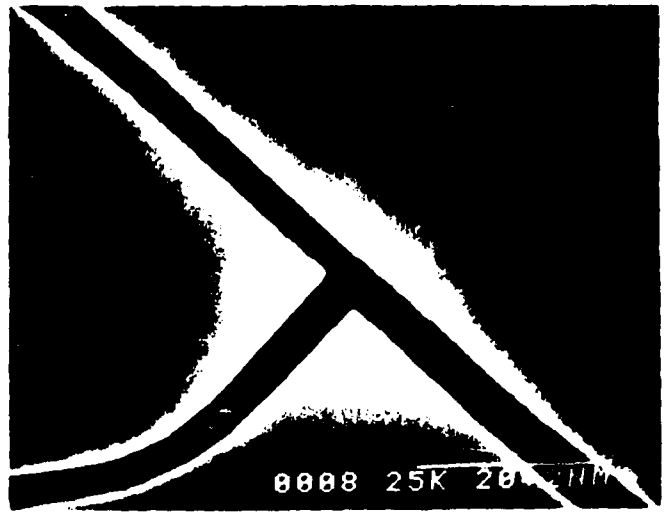

(b) ED-MoS_3(NA)

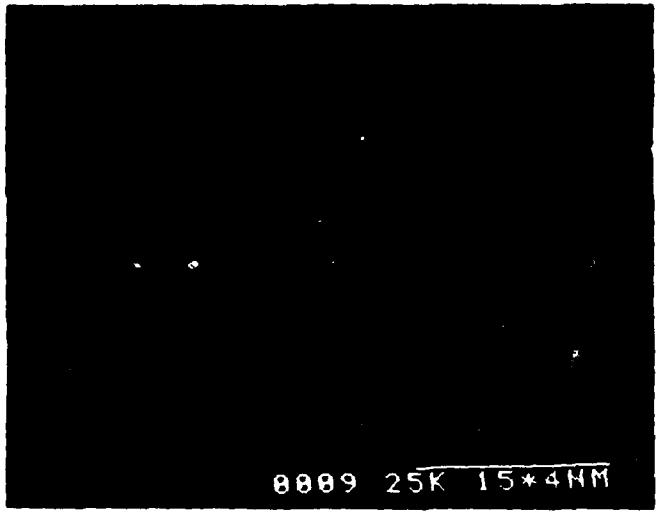

(c) ED-MoS_3(A)

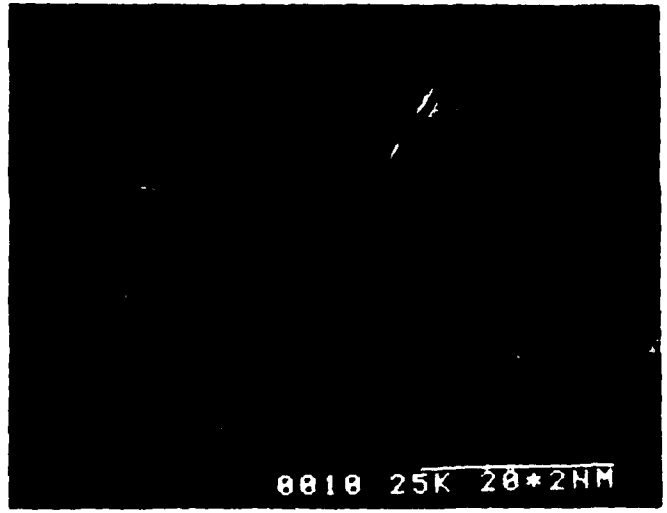

(d) ED-MoS_3(A)

Fig. 24

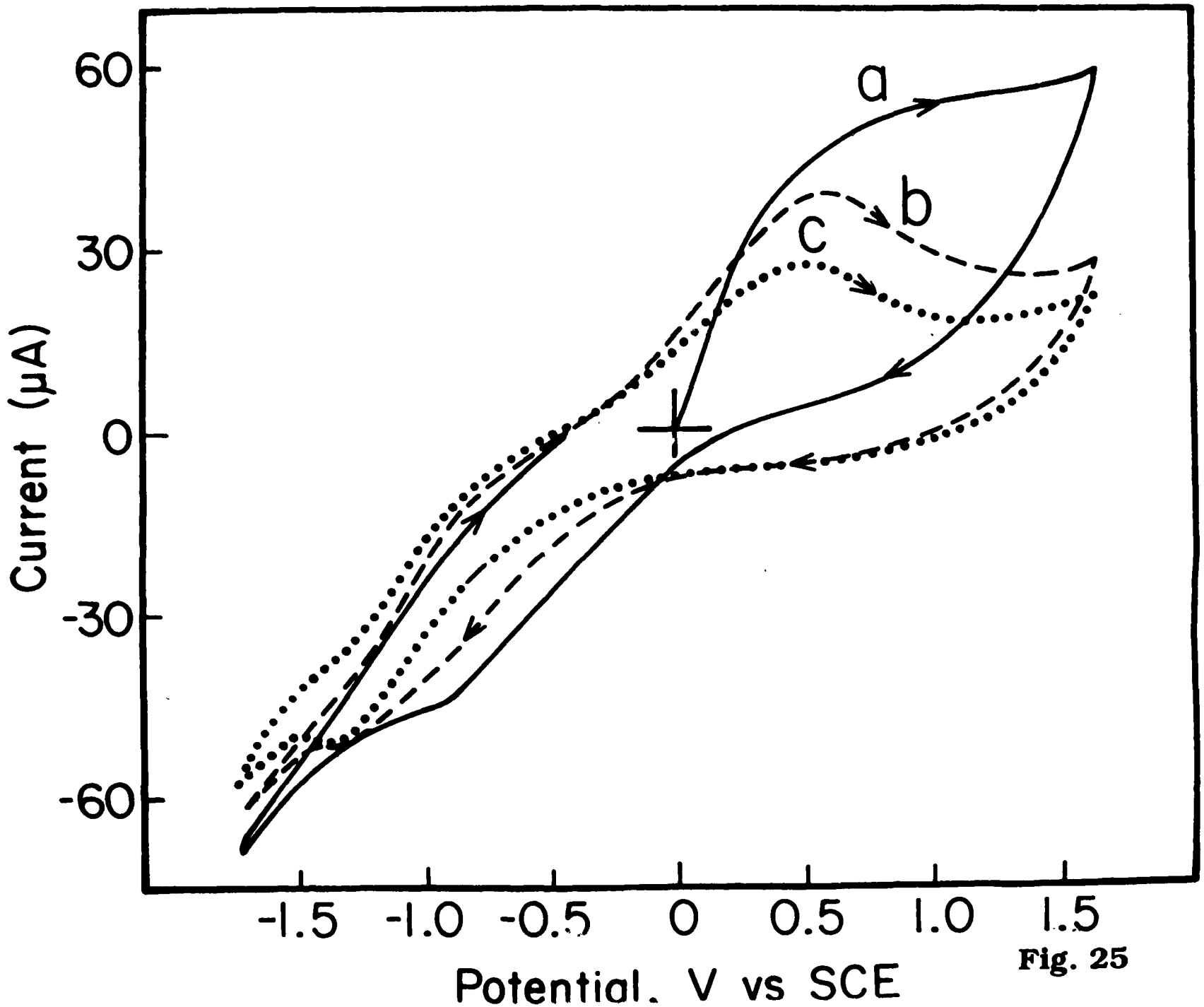

Fig. 25

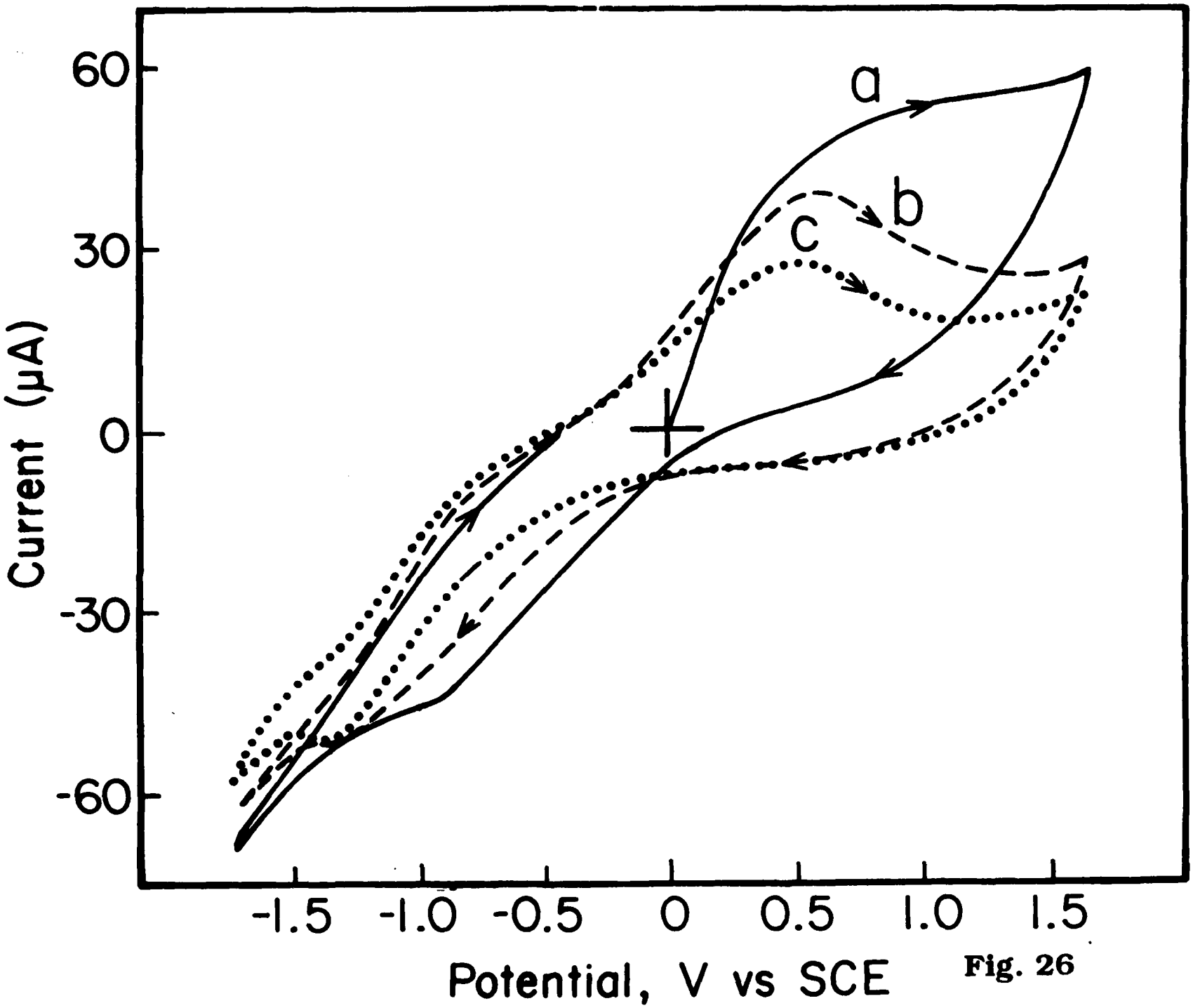

Fig. 26

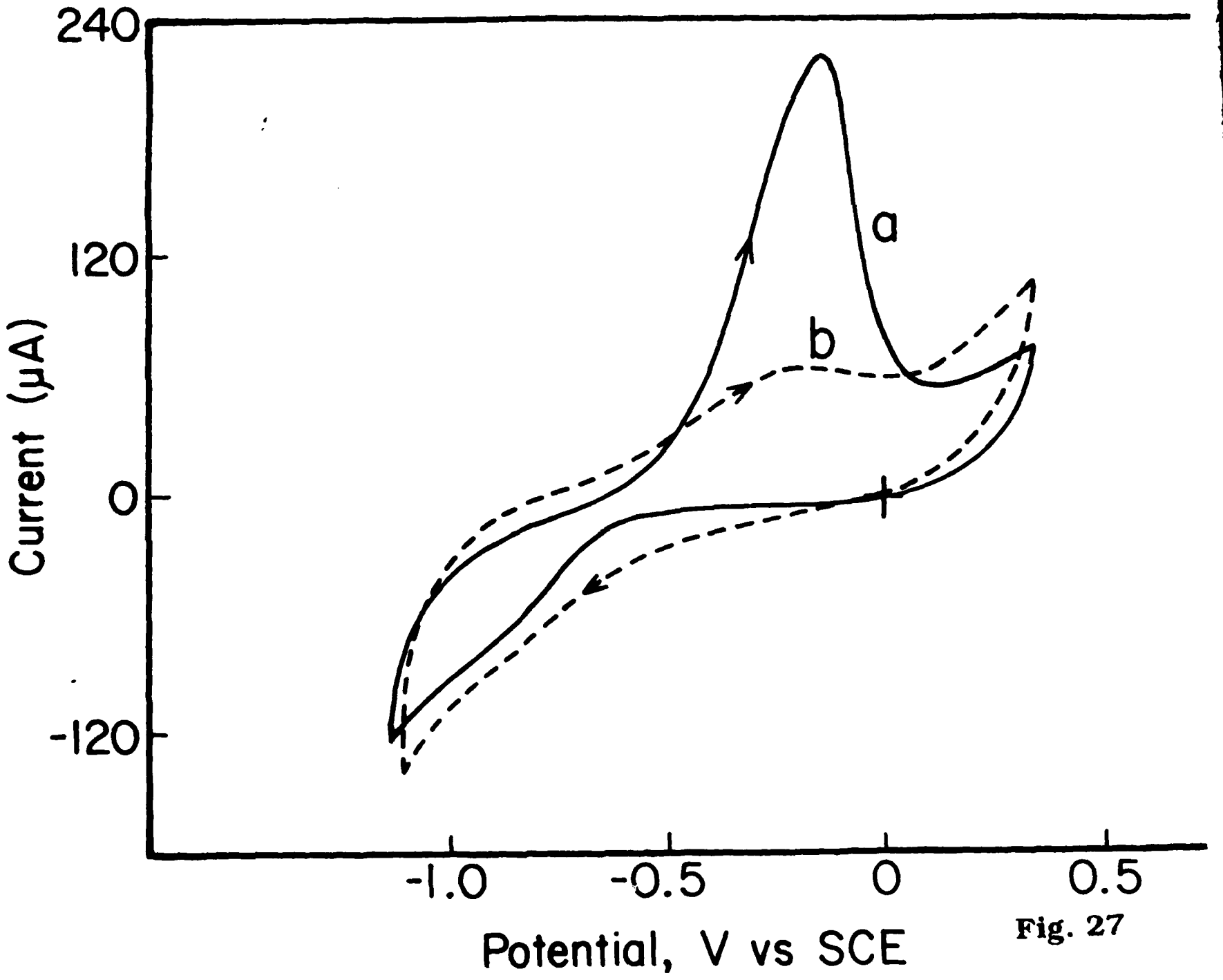

Fig. 27

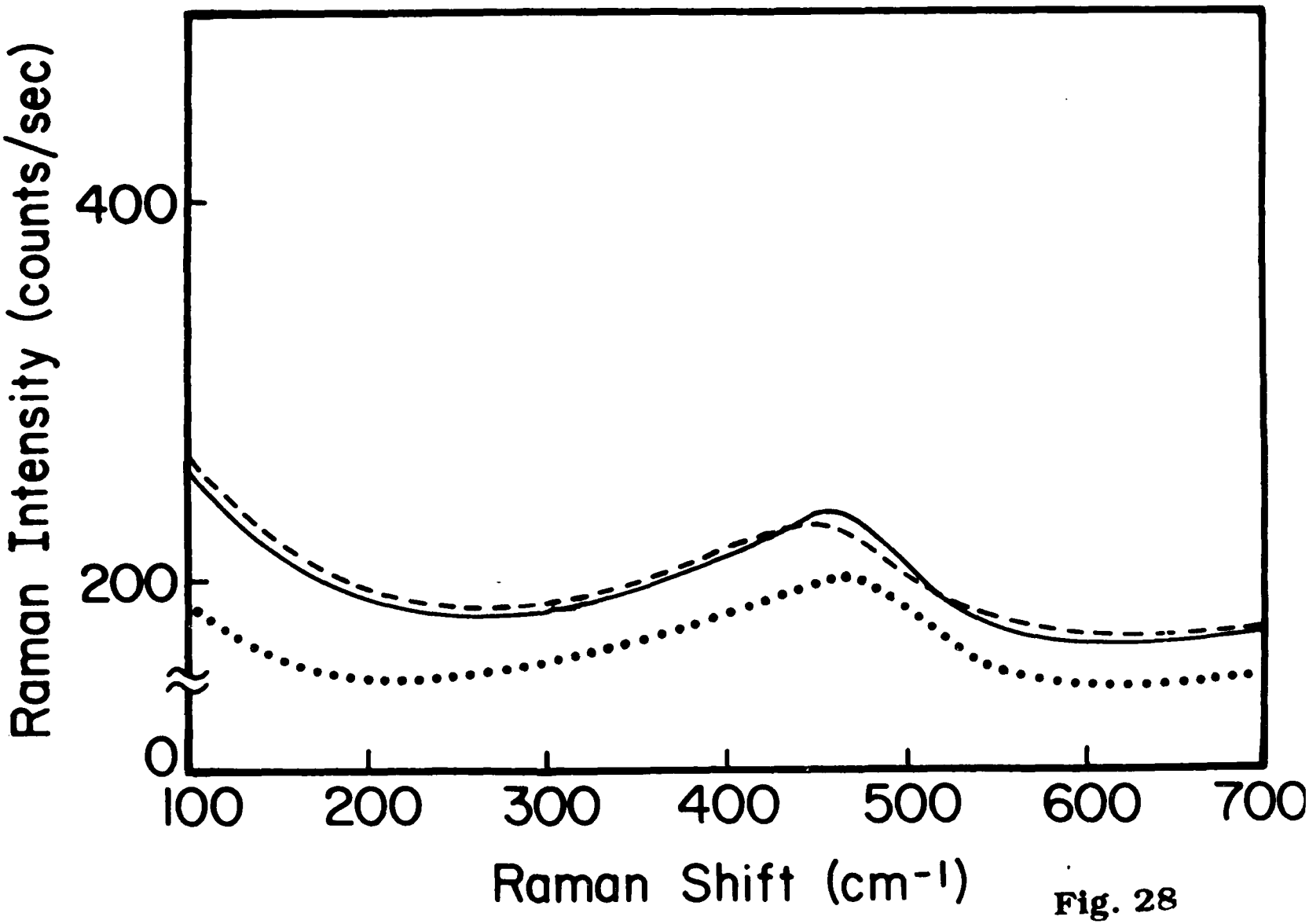
Raman Intensity (counts/sec)
400
200
0
100
200
300
400
500
600
700
Raman Shift (cm⁻¹)

Fig. 28

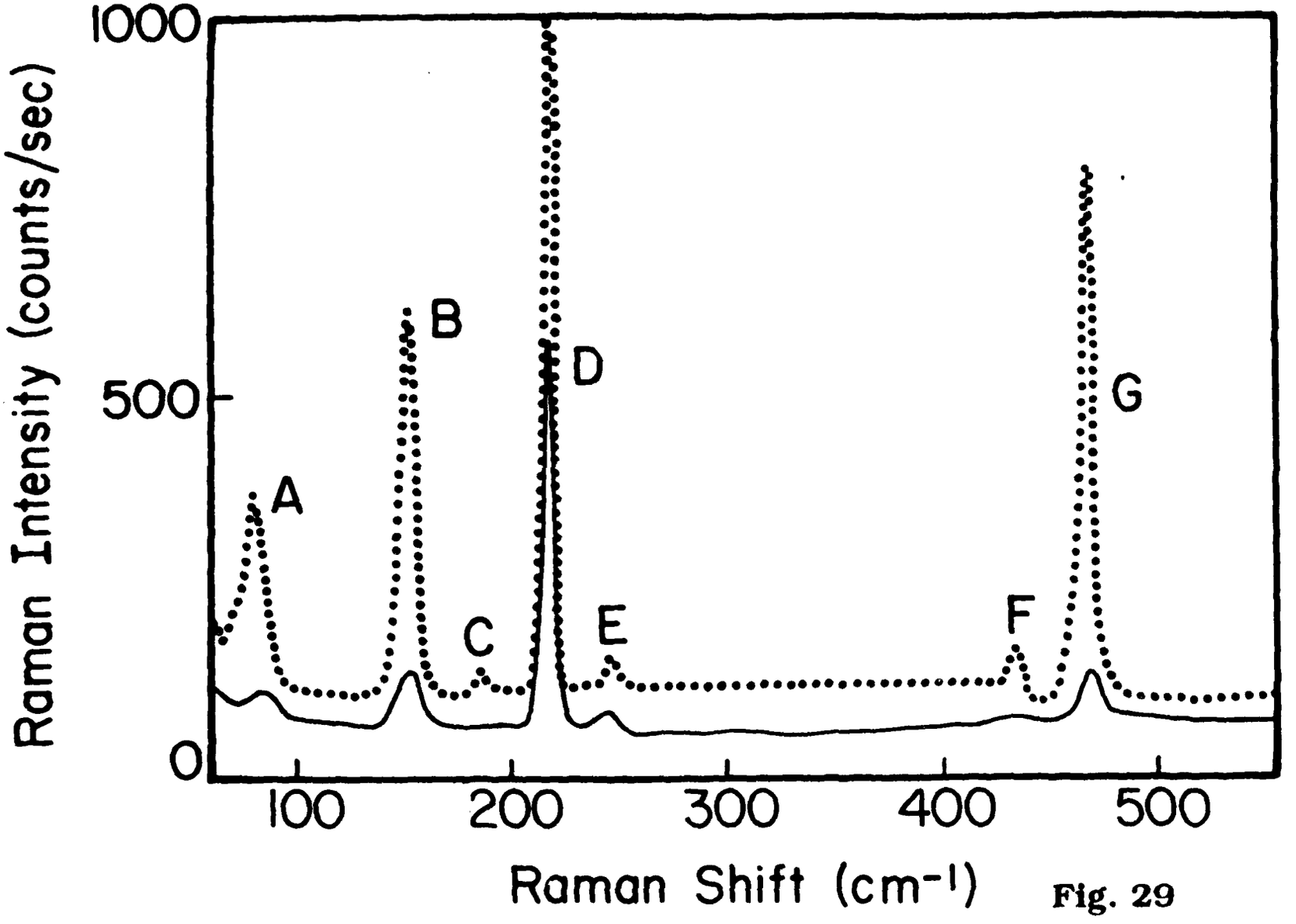
1000
500
0
Raman Intensity (counts/sec)
A
B
C
D
E
F
G
100
200
300
400
500
Raman Shift (cm⁻¹)

Fig. 29

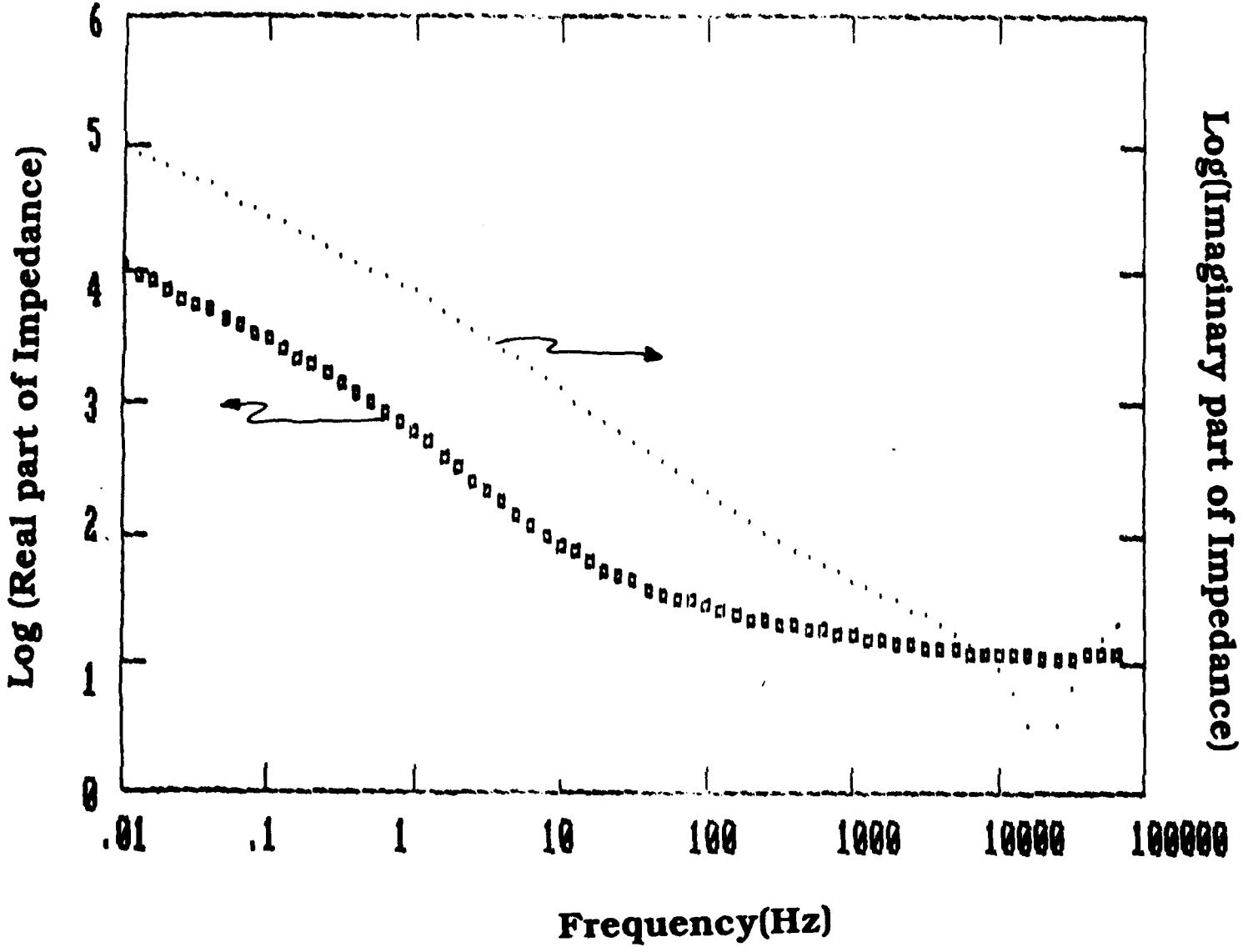
Log (Real part of Impedance)
Log(Imaginary part of Impedance)
6
5
4
3
2
1
0
.01
.1
1
10
100
1000
10000
100000
Frequency(Hz)

Fig. 30

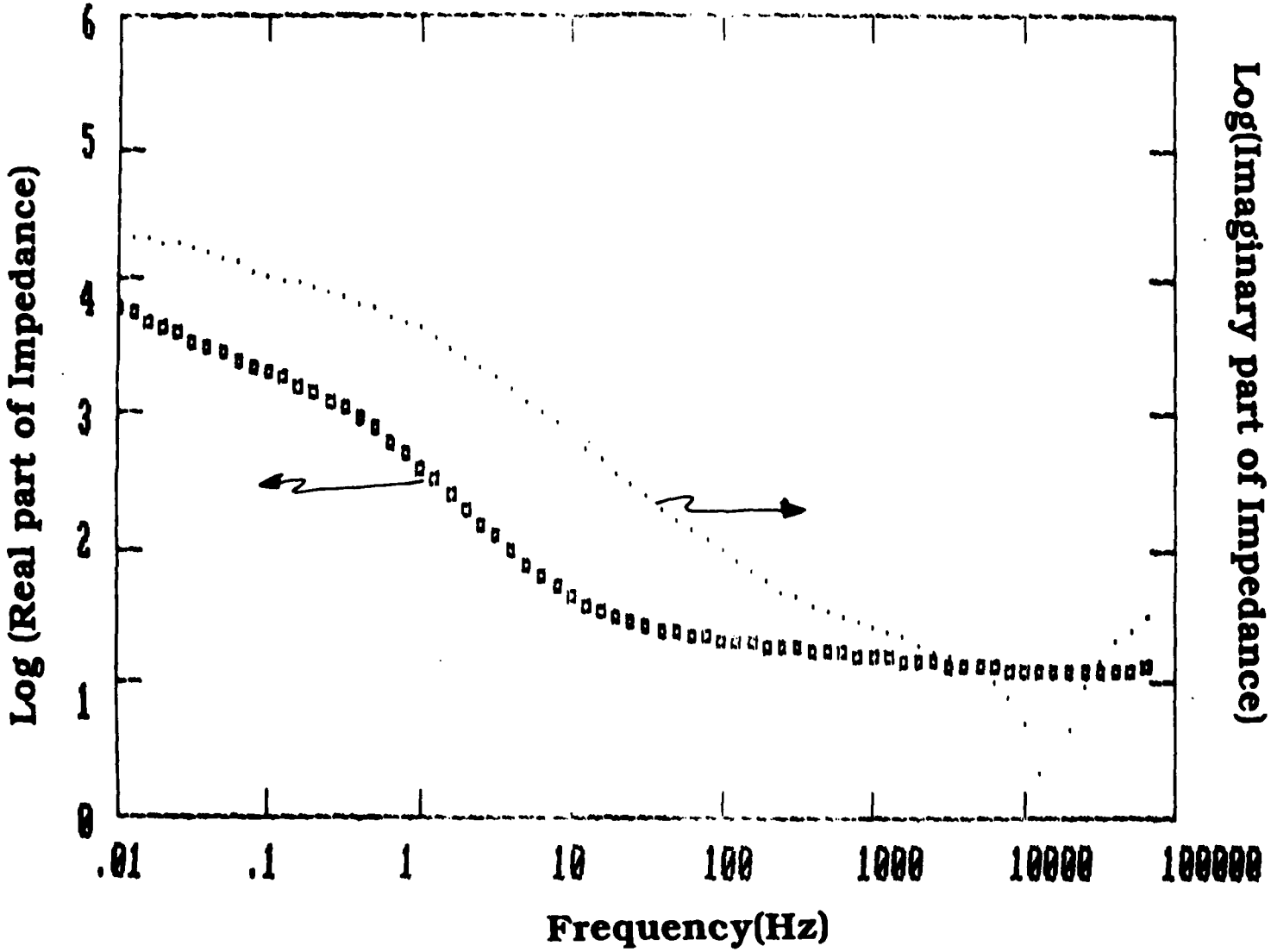
Log (Real part of Impedance)
Log(Imaginary part of Impedance)
6
5
4
3
2
1
0
.01
.1
1
10
100
1000
10000
100000
Frequency(Hz)

Fig. 31

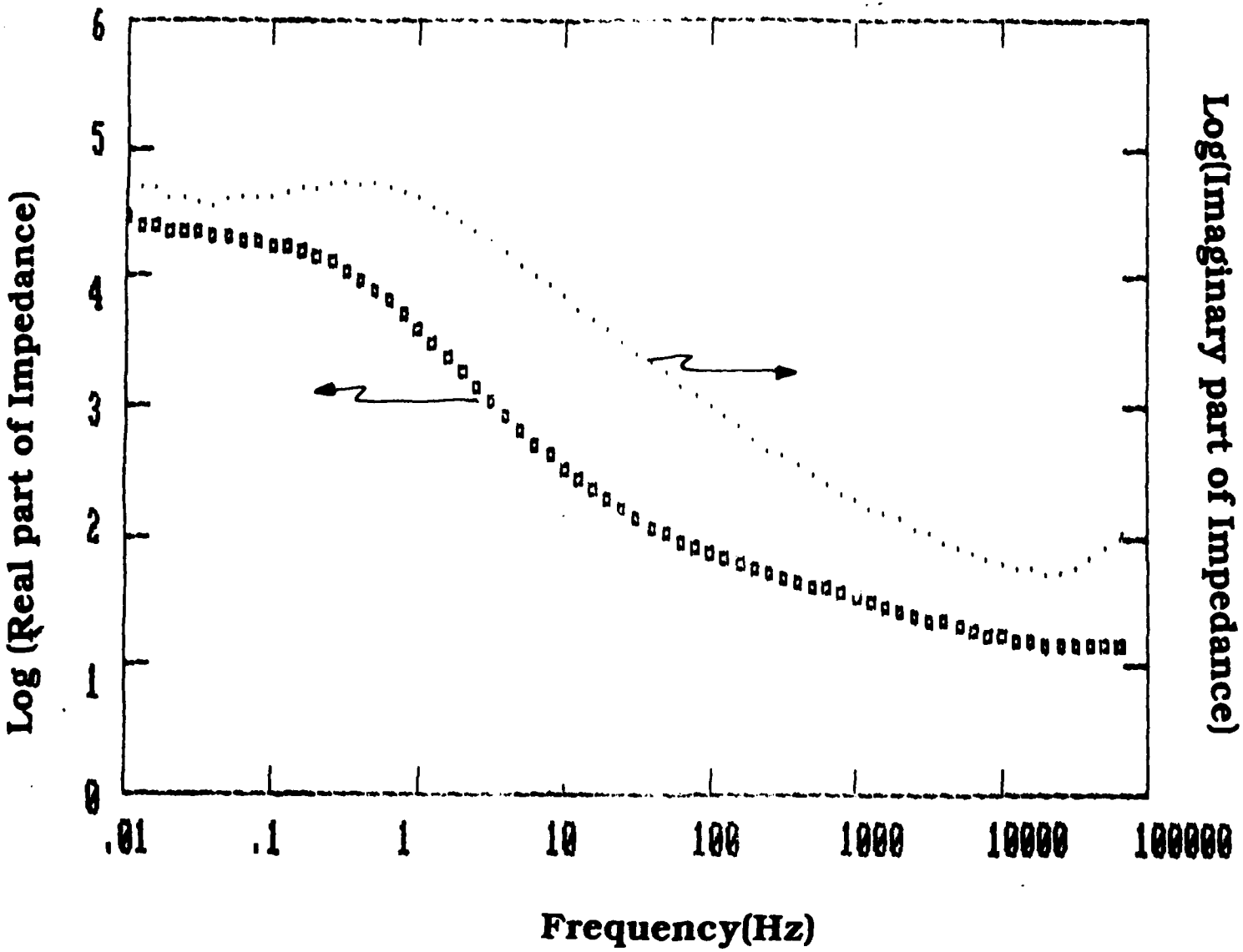
Log (Real part of Impedance)
Log(Imaginary part of Impedance)
6
5
4
3
2
1
0
.01
.1
1
10
100
1000
10000
100000
Frequency(Hz)

Fig. 32

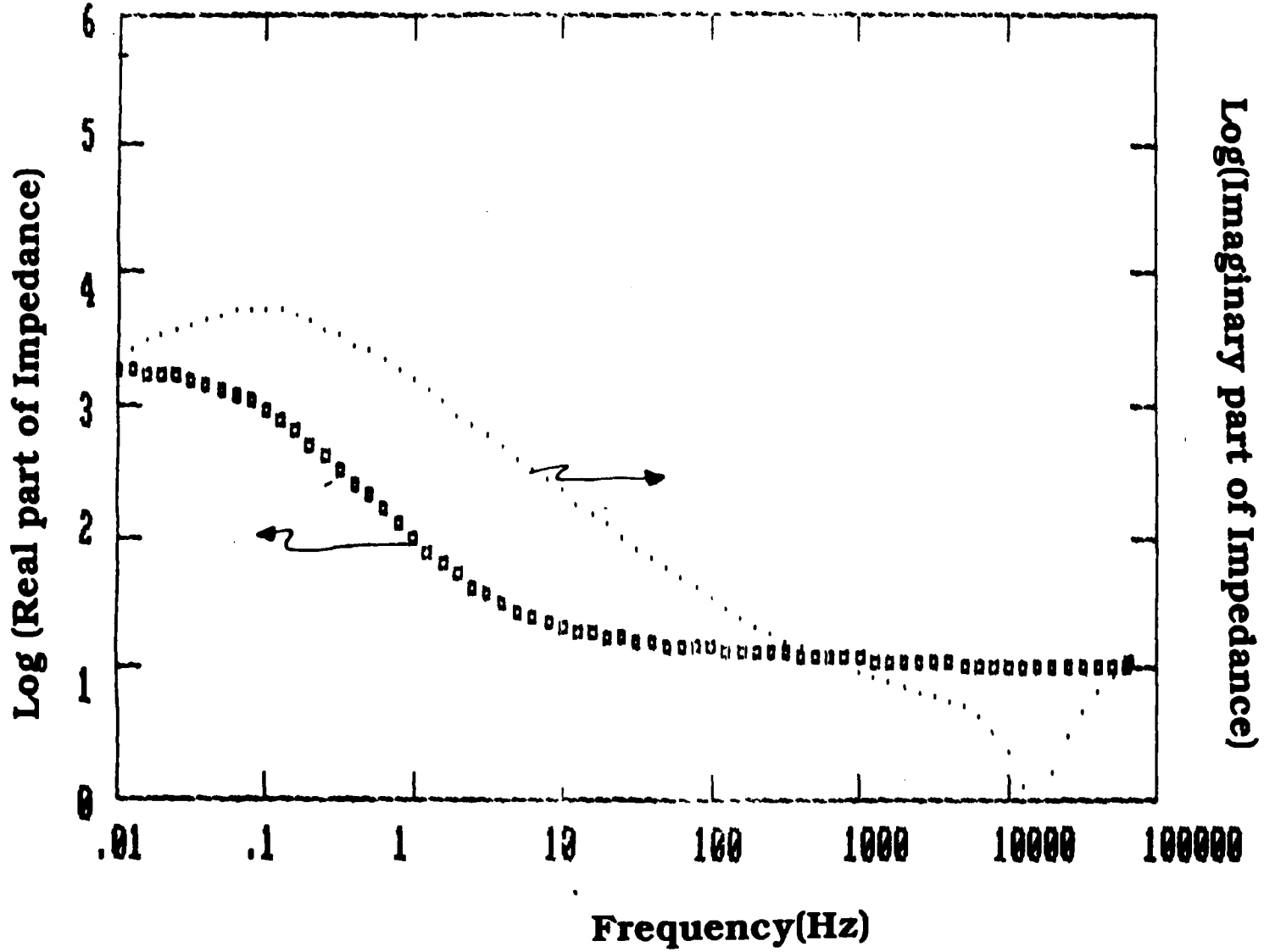
Log (Real part of Impedance)
Log(Imaginary part of Impedance)
6
5
4
3
2
1
0
.01
.1
1
10
100
1000
10000
100000
Frequency(Hz)

Fig. 33

VII. SCIENTIFIC ARTICLES

1. R.N. Bhattacharya, C.Y. Lee, F.H. Pollak and D.M. Schleich in Disorder Semiconductors, ed. by M.A. Kastner, G.A. Thomas and S.R. Ovshinsky (Plenum, New York, 1987) p. 247.

2. R.N. Bhattacharya, C.Y. Lee, F.H. Pollak and D.M. Schleich, J. Non-Crystalline Solids 91, 235 (1987).

3. R.N. Bhattacharya, D.Yan, P.M.S. Lesser, F.H. Pollak and D.M. Schleich, Proceedings of the Symposium on Primary and Secondary Ambient Temperature Lithium Batteries, ed. by J.P. Gabano, Z. Takehara and P. Bro (Electrochemical Society, Princeton, 1988) Vol. 88-6, p. 443.

4. R.N. Bhattacharya, F.H. Pollak, M. Tomkiewicz and D.M. Schleich, submitted to Mat. Res. Bull.